

CM²



MAGAZINE

第 57 期



南方科技大学海洋磁学中心主编

<https://cm2.sustech.edu.cn/>

创刊词

海洋是生命的摇篮，是文明的纽带。地球上最早的生命诞生于海洋，海洋里的生命最终进化成了人类，人类的文化融合又通过海洋得以实现。人因海而兴。

人类对海洋的探索从未停止。从远古时代美丽的神话传说，到麦哲伦的全球航行，再到现代对大洋的科学钻探计划，海洋逐渐从人类敬畏崇拜幻想的精神寄托演变成可以开发利用与科学研究的客观存在。其中，上个世纪与太空探索同步发展的大洋科学钻探计划将人类对海洋的认知推向了崭新的纬度：深海（deep sea）与深时（deep time）。大洋钻探计划让人类知道，奔流不息的大海之下，埋藏的却是亿万年的地球历史。它们记录了地球板块的运动，从而使板块构造学说得到证实；它们记录了地球环境的演变，从而让古海洋学方兴未艾。

在探索海洋的悠久历史中，从大航海时代的导航，到大洋钻探计划中不可或缺的磁性地层学，磁学发挥了不可替代的作用。这不是偶然，因为从微观到宏观，磁性是最基本的物理属性之一，可以说，万物皆有磁性。基于课题组的学科背景和对海洋的理解，我们对海洋的探索以磁学为主要手段，海洋磁学中心因此而生。

海洋磁学中心，简称 CM^2 ，一为其全名“Centre for Marine Magnetism”的缩写，另者恰与爱因斯坦著名的质能方程 $E = MC^2$ 对称，借以表达我们对科学巨匠的敬仰和对科学的不懈追求。

然而科学从来不是单打独斗的产物。我们以磁学为研究海洋的主攻利器，但绝不仅限于磁学。凡与磁学相关的领域均是我们关注的重点。为了跟踪反映国内外地球科学特别是与磁学有关的地球科学领域的最新研究进展，海洋磁学中心特地主办 CM^2 Magazine，以期与各位地球科学工作者相互交流学习、合作共进！

“海洋孕育了生命，联通了世界，促进了发展”。21世纪是海洋科学的时代，由陆向海，让我们携手迈进中国海洋科学的黄金时代

目 录

岩石磁学演绎	1
第 47 章 环境磁学研究的未来	1
文献速递	5
1. 新生代亚洲粉尘来源变化与青藏高原北部和中亚造山带侵蚀历史的联系：来自 Nd 同位素的证据	5
2. 地球中年的造山沉寂	11
3. 俯冲带海洋磁异常的命运：一个全球性的评估	14
4. 地球化学差异反映的地幔深部不同的形成历史	18
5. 不同风化程度好氧土壤对成土过程的磁响应	21
6. 晚中新世之前不能形成现代长江：来自碎屑白云母和钾长石 $^{40}\text{Ar}/^{39}\text{Ar}$ 年代学证据	24
7. 中国黄土高原陆生蜗牛壳体耦合同位素与稳定同位素的气候指示	28
8. 全新世时期海洋驱动和地形控制的非线性冰川撤退：位于南极 Ross Sea 西南部	30
9. 利用岩石磁学对青铜时代 Ada Tepe 金矿场的考古材料进行识别和分类	32
10. 冰消期西南太平洋深海通风变化	34
11. 目前大西洋经向翻转环流是近千年来最弱的	37
12. 硼同位素约束 800 kyr 以来的东亚季风变化	40
13. 重新定义全球变暖的威胁：气候变化、粮食危机和社会崩溃的经验因果循环图	43

岩石磁学演绎

第 47 章 环境磁学研究的未来

综合环境磁学

所有材料在外加磁场作用下都会产生磁响应，所以磁学参数可用来研究许多天然材料和自然过程（气候和环境变化以及许多地质过程）。但是，正如前面讨论的，磁学参数的解释很复杂，所以磁学对气候和环境研究的贡献会随环境、地点和研究重点而变化。例如，在中国黄土/古土壤序列研究中，磁学参数在理解亚洲季风的时空演化过程中起到了主导作用。为了提高环境磁学的重要性和目的性，必须清楚什么情况下磁学性质可以为环境过程提供有用的指标，而什么情况只是作为一种辅助方法为其他方法提供一个证据而已。尽管在复杂的环境系统中，因果的区分并不都是明确的，但是在很多情况下比较恰当的思路是，先利用最有效的指标（如稳定同位素、动物群、植物群等）来重建气候，然后利用磁学方法来确定气候变化的影响。

在研究新的环境、应用、时间尺度和沉积记录时，需要将磁学参数和其他环境气候参数同时研究。这种多学科结合的方法不仅仅是磁学与非磁学指标的结合，而是不同专家之间的全面讨论。例如，经过了十多年的研究才确定了中国黄土/古土壤序列中古土壤层 χ 增强的具体机制[Zhou et al., 1990; Liu et al., 2007a]。鉴于湖泊沉积物为复杂的磁性矿物混合，并且经历了一系列会影响磁学参数的环境气候过程，所以多参数指标结合对于湖泊沉积物的研究同样重要。所以，未来的环境磁学研究应该注重多学科结合。例如，在研究海洋沉积物的粉尘输入时，剩磁的硬磁组分、漫反射光谱（DRS）、地球化学指标（如 Ti/Al）、非磁性组分的矿物分析（如粘土矿物、石英）等各参数的有机结合可以有效地分析粉尘物质并追踪其物源。另外，建立新的分析和统计方法也是十分必要的。对于针铁矿和赤铁矿的研究，除非它们的物源和固有磁学性质是稳定的，否则硬磁组分含量的指标是变化的。DRS 方法可以对这两种矿物进行有效的定性和定量化研究，但是 DRS 会受到铝替代的严重影响[Liu et al., 2011]，所以在利用 DRS 对赤铁矿和针铁矿进行定量化研究时，需要特别注意这种影响。

未来的研究包含不同生物气候带之间的转换位置。为了加深对环境理解，物源分析是十分必要的。那么，采点位置的选取需要更加精确以使源区的环境变化达到最小，这样才能更好的解释气候变量的环境信息。

环境磁学的优点在于磁学测量的快捷，因此可以相对简便的得到大量的高分辨率数据。所以，环境磁学适合快速监测局部或者全球尺度的污染，或者其他环境过程如粉尘运输[Maher et al., 2010]。纳米颗粒的磁学性质变化十分明显，所以磁学参数可用来研究混

合磁性矿物的特征，以提供物源和环境过程的信息。另外，磁学测量还可以提供其他传统方法（如 XRD，地球化学分析）测量范围之外的信息，定量化研究含量较低的亚铁磁性和反铁磁性矿物的相对关系。

黄土/古土壤的研究展望

未来黄土/古土壤序列的环境磁学研究需要解决两个重要的问题，首先，深入探索成土作用过程磁性矿物的形成和转化机制，其次，黄土磁学的古气候意义需要更详细的研究，尤其是对于全球气候变化和区域性变化的解释。关于第一个问题，基本问题是为什么季节性干燥的土壤会保持足够长时间的湿润环境来生成 Fe^{2+} ，进而产生少量的磁铁矿或磁赤铁矿。并没有完全干燥的地中海土壤（ Fe^{2+} 形生于冬季）含有大量的针铁矿，但是几乎没有赤铁矿和磁赤铁矿。所以，成土作用过程中磁性矿物的转化需要深入研究。由于成土作用形成的中间磁性矿物矿物相并不存在，所以结合实验测量或者数值模拟得到的矿物学、磁学以及气候参数（Hm/Gt、Hm/Mag 随温度和降水的变化）共同分析，可以得到磁性矿物的形成机制。关于第二个问题，尽管将黄土和全球的其他粉尘记录进行比较只能帮助我们区分全球的和区域性的动力学机制，但是可以加深我们对全球尺度上大气变化的理解[Roberts et al., 2011c]。另外，对于黄土的物源分析对于我们建立综合的传输和沉积后改造模型是十分必要的。

其它陆内沉积物的研究展望

湖泊沉积物的优点在于可以记录反映人类活动历史的局部信息，应重点加强古环境和古地磁研究。由于河流相和冲积相沉积物可以提供陆内区域上（如半干旱气候带）和时间尺度上（如晚第三纪和第四纪）的环境变化记录，所以对它们的多指标研究变得越来越重要。另外，物源分析对于理解海洋和湖泊沉积物的沉积记录也是十分重要的。人烟稀少地区松散的表层沉积物和冰盖/冰川也是粉尘物源研究的良好介质，同时洞穴的环境磁学研究也是未来的一个重要领域。

海洋沉积物研究展望

尽管河流在铁循环和碳循环中起到了很重要的作用，但是与其它陆源物源相比，对海洋沉积物中河流输入的研究是很匮乏的[Raiswell et al., 2006]。对于沉积物漂流的环境磁学研究为入海口热盐循环、地质结构的研究提供了重要的思路。由于河流的供给和底

层流对沉积物的再改造,因此慎重选取研究位置,全面了解源区信息是十分重要的。关于冰川输入的陆源物质,环境磁学研究不仅需要解决晚第三纪和第四纪的冰盖的动力机制,而且要提供“冰库”时期的冰盖信息和暖期小冰体存在的可能性。

大部分“冰库”时期的信息,尤其是早第三纪之前的,主要是基于对粗粒混杂沉积物的研究[Eyles, 1993]。同时期 IRD 携带的细粒沉积物的环境磁学研究为古代冰盖的范围和动力学机制提供了许多新思路。靠近南极的海洋沉积物中 IRD 层的信息表明[Ehrmann and Mackensen, 1992; Williams et al., 2010],南极洲从最早的渐新世开始就已经永久冻结了[e.g., Zachos et al., 2001]。IRD 沉积记录恰好在现今极锋(大约 50°S)的南部,所以环南极的海洋沉积物环境磁学研究可以提供南极冰盖的动力学信息[Kanfoush et al., 2002]。

大气粉尘是气候变化的重要响应,但是第四纪期间它在全球气候中的作用仍然知之甚少,何况更早的时期 [Maher et al., 2010]。所以,对于海洋沉积物中风成粉尘的环境磁学研究变得越来越重要,尤其是考虑到磁性矿物在识别风成粉尘及确定驱动其形成的环境变量的有效性。另外,前人研究表明风成粉尘也可以和生物成因的磁铁矿共存[Bloemendal et al., 1992; Yamazaki and Ioka, 1997b; Dinarès-Turell et al., 2003; Yamazaki, 2009; Abrajevitch and Kodama, 2011; Roberts et al., 2011b; Larrasoña et al., 2012]。尽管对粉尘和趋磁细菌的可能联系并没有进行详细的研究,但是它们的共存说明它们之间可能存在一些因果关系,粉尘可能为生物矿化提供了反应铁[Roberts et al., 2011b; Larrasoña et al., 2012]。鉴于生物成因的磁铁矿和氧化还原环境的瞬间变化,为了更好地理解控制海洋沉积物中生物成因磁铁矿的形成及保存因素,需要对瞬间暖期的沉积物进行研究,如早第三纪高热(PETM)事件和中生代大洋缺氧事件(OAEs)。

关于沉积后成岩作用的变化,磁性矿物的还原溶解、胶黄铁矿的保存更多的用来解释氧化还原条件的变化,尽管它们还和冰盖的变化(高纬度地区)、底层流的流动(尤其是半封闭盆地)、河流输入的变化以及其它因素有关。环境磁学的另一个比较有前景的应用是,利用成岩作用形成的黄铁矿和胶黄铁矿来研究古海洋沉积物中天然气水合物的存在[Housen and Musgrave, 1996; Larrasoña et al., 2007; Enkin et al., 2007; Roberts et al., 2010]。天然气水合物的稳定性在推动和响应某些气候事件中起了重要作用,而前人对于天然气水合物的研究为这些重要事件提供了新的思路,例如 PETM 事件,天然气水合物的突然解体导致碳循环的混乱,进而推动了全球变暖 [Zachos et al., 2001]。

白垩纪的大洋红层是对有氧条件下沉积后成岩作用进行环境磁学研究的主要介质,主要为 OAEs 事件之间的海洋沉积岩。这些沉积物记录了中白垩与晚白垩期间全球变冷的主要气候变化,但目前对于这些沉积物并没有详细的研究[Wang et al., 2011]。白垩纪大洋红层的主要载磁矿物为早期成岩作用形成的赤铁矿和针铁矿,随洋底有机碳供给和底层流氧化情况的变化而变化[Li et al., 2011],所以很适合做环境磁学分析。

生物成因磁性矿物的研究展望

未来生物矿化研究主要集中于一些基本问题：生物成因磁性矿物的可靠鉴别、生物矿化过程和生物成因磁性矿物的环境信息提取。前人提出了一些鉴别生物成因磁铁矿的磁学标准，如低温的 Moskowitz-test [Moskowitz *et al.*, 1993]、FORC 图中典型的无相互作用的 SD 磁铁矿[Egli *et al.*, 2010]，但是这些标准并不能准确鉴别生物成因磁铁矿，在某种程度上是因为磁小体链会断开或者被氧化[Li *et al.*, 2010; Kind *et al.*, 2011]。测量生物成因和非生物成因的磁性矿物的铁同位素信息可以帮助鉴别这两种成因的磁性矿物[Anbar *et al.*, 2000]。确定环境因素对磁小体形成的控制对于理解生物矿化过程的动力学机制是十分必要的。同样地，利用不同形状的磁小体化石来研究古环境记录也需要对现今环境中不同氧化还原梯度下趋磁细菌种类的空间分布进行深入研究。生物矿化研究的另外一个应用在于其对基础岩石磁学的贡献。Cao *et al.* [2010] 利用重组的人类 H 链铁蛋白合成了理想的无相互作用的纳米级铁蛋白。这种材料加深了对超顺磁系统的研究，对环境磁学研究具有十分重要的作用。

结束语

在过去的 30 年，环境磁学取得了飞速发展，已成为一门复杂的定量化学学科。随着该学科的逐渐成熟，先进的实验和数据分析技术的出现，以及对越来越多磁性材料磁学性质的深入理解，环境磁学已被用于解决许多重要问题。尽管在磁学性质的解释中仍存在不确定性，甚至在解决一些复杂环境问题中仍存在挑战，但是解决这些难题的方法会逐渐增多。总之，我们对多学科结合的环境磁学的未来充满希望，其必将增强磁学在环境科学中的重要性。

1. 新生代亚洲粉尘来源变化与青藏高原北部和中亚造山带侵蚀历史的联系：来自 Nd 同位素的证据

翻译人：仲义 zhongy@sustech.edu.cn



*Yang, Y B, Galy, A, Fang, X M, et al. Neodymium isotopic constraints on Cenozoic Asian dust provenance changes linked to the exhumation history of the northern Tibetan Plateau and the Central Asian Orogenic Belt [J] *Geochimica et Cosmochimica Acta*, 2021, 296, 38-55.*

<http://www.sciencedirect.com/science/article/pii/S0016703720307390>

摘要：亚洲大陆的干旱区是北太平洋风尘沉积的最大来源，同时一些风尘甚至被输送到格陵兰岛。研究亚洲风尘源区历史可以为亚洲内陆的地形和气候演化提供有力的约束。40 Ma 以来北太平洋地区风尘 Nd 同位素可以为亚洲源区变化提供一级空间控制，然而，在亚洲风尘源区，即青藏高原北部和中部地区缺乏类似的长时间的风尘 Nd 同位素记录，该研究对于理解亚洲内陆新生代构造、气候和地形演化的全面认识。本文中，我们重建了青藏高原北部 52 Ma 以来的细粒和全岩的 Nd 同位素结果。结果显示出两次重要的改变，Nd 同位素 42 Ma 和 25 Ma 之间呈现出逐渐升高，而从 25 Ma 总体开始下降，该变化可能是由于青藏高原北向抬升有关。进而，通过对比青藏高原北部和北太平洋风尘 Nd 同位素的质量平衡计算，显示出 25Ma 以来中亚造山带作用对亚洲风尘升高，其成因与亚洲内陆构造隆升和干旱化引起的剥蚀有关。结合东亚和中亚风尘沉积物的初始形成风尘，作者认为从晚渐新世以来，一种类似现代的机制已经形成，促进了亚洲风尘排放和输送。

ABSTRACT: The arid interior of Asia is the largest source of dust deposited in the North Pacific Ocean, and some dust is even transported to Greenland. Investigating the provenance history of Asian dust can provide strong constraints on the evolution of topography and climate in the Asian interior. Eolian dust Nd isotopic records preserved in North Pacific Ocean sediments since 40 Ma provide a spatially integrated first-order constraint on the provenance changes of Asian dust. However, a lack of similarly long dust Nd isotopic records from Asian dust source areas, namely, the northern Tibetan Plateau and the Central Asian Orogenic Belt, has hindered a full understanding of Asian dust provenance changes linked to the Cenozoic evolution of tectonics, climate and

topography in inland Asia. Here, we have constructed the first fine-grained and whole-rock Nd isotopic records from sediments deposited on the northern Tibetan Plateau since 52 Ma. The results indicate two major changes, a gradual increase in $\epsilon\text{Nd}(0)$ values between 42 Ma and 25 Ma and a general decrease since 25 Ma, which were probably caused by the incremental northward growth of the Tibetan Plateau. Further mass balance estimates based on comparisons between the Nd isotopic characteristics of dust from the northern Tibetan Plateau and the North Pacific Ocean indicate that a rapid increase in the contribution of the Central Asian Orogenic Belt to Asian dust at 25 Ma can be closely linked to rapid exhumation caused by tectonic uplift and aridification in inland Asia. Our provenance analyses, together with the onset of eolian sediment in central and eastern Asia, suggest that a modern-like regime promoting Asian dust emissions and transport might have been in place since the late Oligocene.

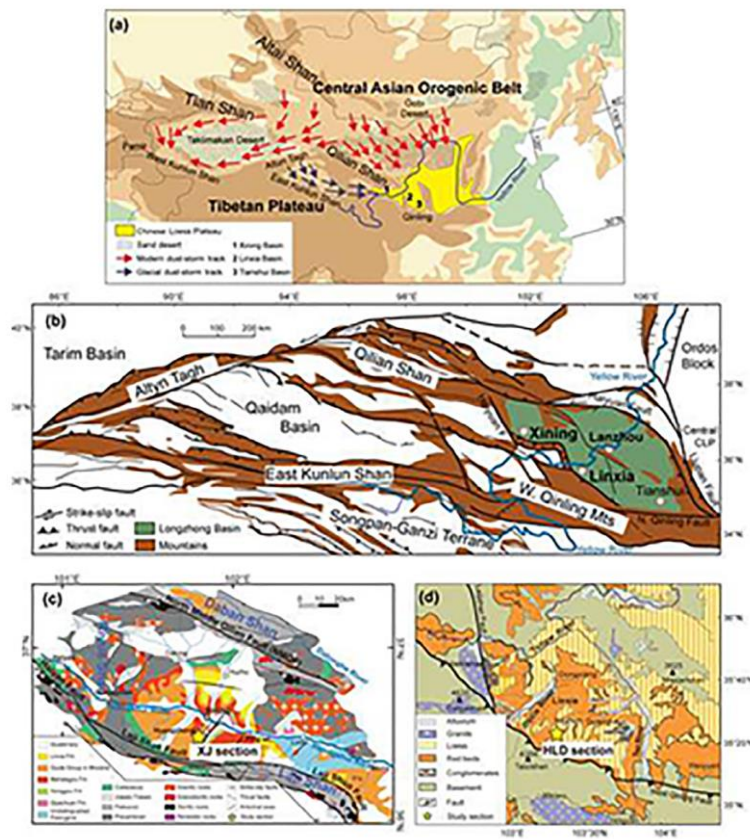


Figure 1. Map of the study areas. (a) Map of central and eastern Asia, showing the modern, simplified dust storm tracks and near-surface wind patterns (red arrows) and the hypothetical “glacial” dust storm tracks (blue arrows) to the Chinese Loess Plateau (CLP) (redrawn from Licht

et al., 2016) with the locations of the Linxia and Xining (this study) and Tianshui Basins (Chen and Li, 2013). (b) Structural map of the Longzhong Basin on the northeastern Tibetan Plateau (redrawn from Dai et al. 2006). Geological map of the Xining Basin (c) and Linxia Basin (d), showing the surrounding mountains, major structures, and yellow star indicating the locations of the studied XJ and HLD sections (redrawn from Dai et al., 2006, and Fan et al., 2006). (For interpretation of the references to colour in this figure legend, the reader is referred to the web version of this article.)

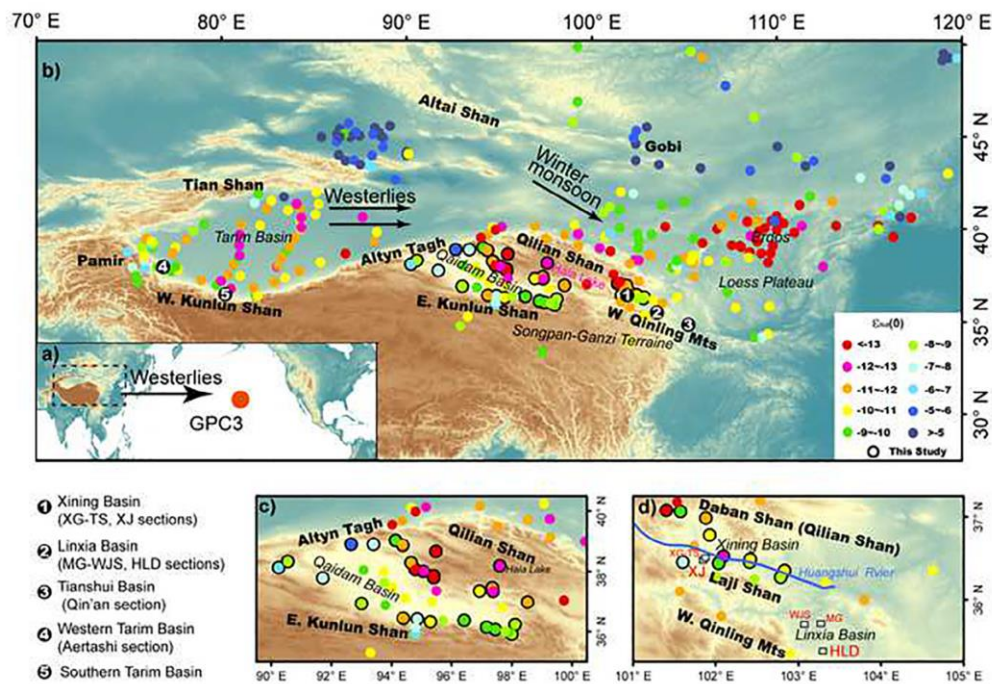


Figure 2. Map showing the modern distribution of Nd isotopic compositions expressed in eNd(0) values for various surface sediments in northern China and Mongolia. (a) Map showing Asian dust source areas and the GPC3 borehole in the North Pacific Ocean. (b) Zoomed-inmap of the dashed black rectangle in (a). The two enlarged maps show the Nd isotopic distribution around the Qaidam Basin (c) and the Xining Basin (d). Note that the dots with black outlines are from this study; other data are from surface sediments (desert, fluvial, moraine, and loess samples) and soils (Blayney et al., 2019; Chang et al., 2000; Chen et al., 2007; Clift et al., 2017; Garziona et al., 2005; He et al., 2019; Li et al., 2009; Liu et al., 1994; Nakano et al., 2004; Rao et al., 2015; Wu et al., 2010; Zhao et al., 2014, 2015).

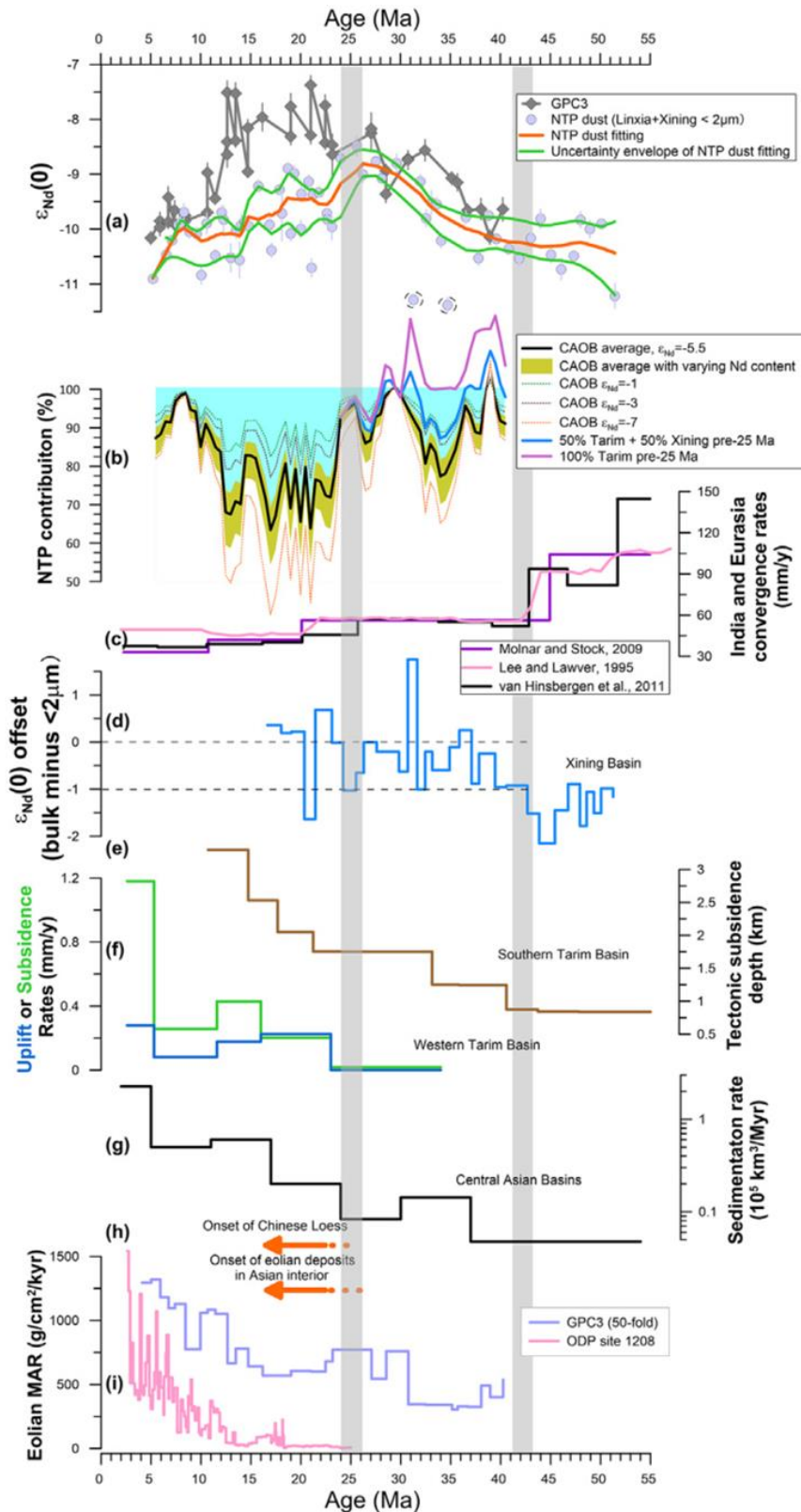


Figure 3. The reconstructed Cenozoic eolian dust Nd isotopic variations (expressed in $\epsilon_{Nd}(0)$ values) in the NTP and their comparison with other records. (a) Dust $\epsilon_{Nd}(0)$ values in the NTP and core GPC3. For the NTP, the bold orange curve represents the locally weighted scatterplot

smoothing (LOWESS, smoothing factor is 0.15) fitting of the NTP dust data from the Nd isotopic compositions of the < 2 μm fraction in the Linxia and Xining Basins, and the green curve represents the uncertainty envelope (note that the two very negative data with dashed circles at 30–36 Ma have been excluded for the composite curve). (b) The NTP contributions to the NPO dust estimated by mass balance by equation (1) using NTP and NPO records and assuming a constant CAOB Nd composition in various scenarios (CAOB ϵNd values of 1, 3, 7, and 5.5). The black line denotes the NTP contribution estimated by the ϵNd mean value of 5.5 for the < 2 μm fraction of the CAOB surface sediments (Table S3). The yellow shaded area shows the uncertainty envelope of varying Nd concentrations (1 σ change in Nd mean concentration of < 2 μm fraction of the CAOB surface sediments, from 24 to 46 $\mu\text{g/g}$, Table S3) corresponding to CAOB ϵNd values of 5.5. The CAOB contribution of the western Tarim Basin (for the period between 38 and 30 Ma) to NPO dust is shown by the light blue area. Two sensitivity tests for the Tarim Basin contribution before 25 Ma are shown in the bold blue (Tarim Basin represents 100% of the NTP contribution) and violet lines (Tarim Basin represents 50% of the NTP contribution). (c) Convergence rates between India and Eurasia (Lee and Lawver, 1995; Molnar and Stock, 2009; van Hinsbergen et al., 2011). (d) Offset in the $\epsilon\text{Nd}(0)$ values between the bulk sediment and the < 2 μm fraction in the XJ section of the Xining Basin. (e) Tectonic subsidence depth in the Aertashi section in the western Tarim Basin (Blayney et al., 2019). (f) Average uplift (blue line) and subsidence (green line) rates in the southern Tarim Basin (Jiang and Li, 2014). (g) Sediment accumulation rate in central Asia (Me'tivier and Gaudemer, 1999). (h) The onset of eolian sediment development (orange arrows) in central Asia (Sun et al., 2010; Zheng et al., 2015) and in the CLP (Guo et al., 2002; Qiang et al., 2011). (i) Eolian mass accumulation rate (MAR) at DP site 1208 (Zhang et al., 2016) and in core GPC3 (Janecek and Rea, 1983). To show the variations in the two records on the same graph, the GPC3 data have been blown up 50 times. The vertical gray bars mark the two transition periods of 42 Ma and 25 Ma. For interpretation of the references to colour in this figure legend, the reader is referred to the web version of this article.)

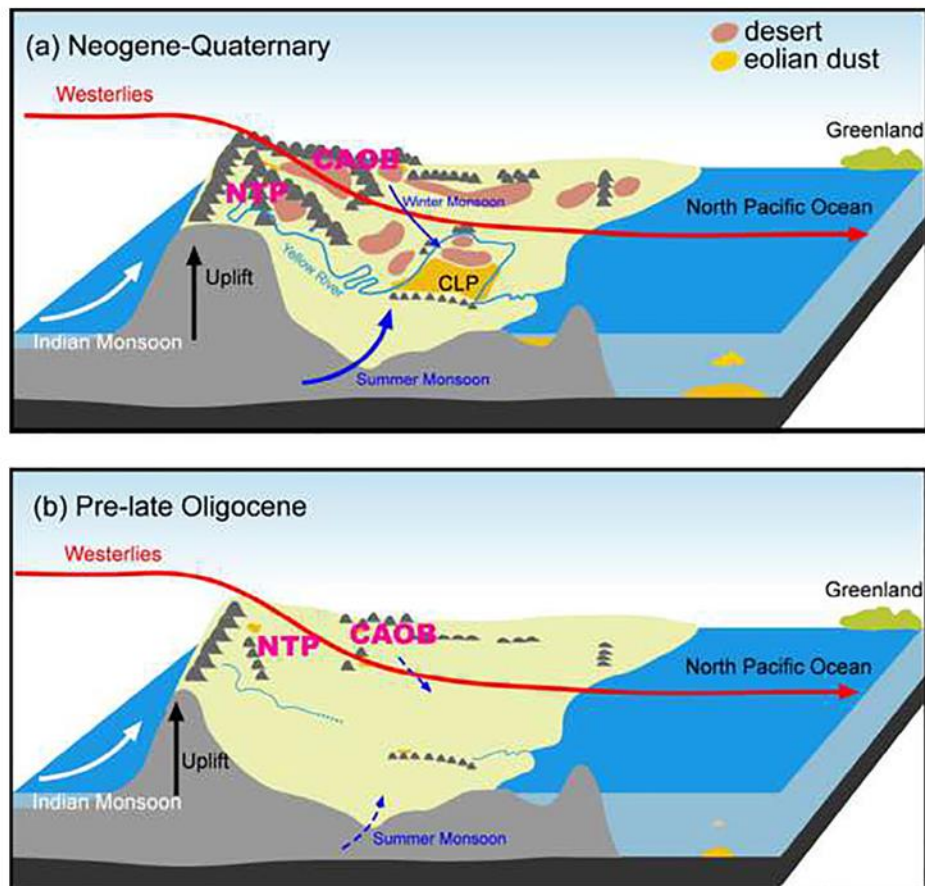


Figure 4. Schematic diagram of Asian dust production and transport from the NTP and CAOB regions to the proximal CLP, the distal North Pacific and even Greenland. (a) The Neogene-Quaternary regime (modified after Chen and Li, 2011 with tectonically active NTP and CAOB regions in combination with a strong East Asian monsoon system). (b) The regime prior to the late Oligocene (further modified from (a) with high elevations in south-central Tibet but a less tectonically active NTP and a relatively low-relief CAOB).

2. 地球中年的造山沉寂

翻译人: 冯婉仪 fengwy@sustech.edu.cn



Tang M, Chu X, Hao JH, et al. *Orogenic quiescence in Earth's middle age [J]. Science, 2021, 371, 728-731.*

<https://doi.org/10.1126/science.abf1876>

摘要: 造山带控制着大陆的剥蚀通量和水文过程, 因此是地球表面营养元素循环的基础。我们利用碎屑锆石中的铕异常来示踪地球历史上的造山过程。研究表明, 活跃的大陆地壳的平均厚度在十亿年的时间尺度上发生了变化, 其中最厚的地壳形成于太古宙和显生宙。而在元古宙, 地壳厚度不断降低, 直到元古宙末期, 大陆都没有高山。我们将这种逐渐减弱的造山作用与长期存在的 Nuna-Rodinia 超大陆联系起来, 该超大陆改变了地幔热结构并且使大陆岩石圈减薄。这一长时间的造山沉寂可能导致了海洋营养元素的持续匮乏, 并阻碍了地球中年时期生命的进化。

ABSTRACT: Mountain belts modulate denudation flux and hydrologic processes and are thus fundamental to nutrient cycling on Earth's surface. We used europium anomalies in detrital zircons to track mountain-building processes over Earth's history. We show that the average thickness of active continental crust varied on billion-year time scales, with the thickest crust formed in the Archean and Phanerozoic. By contrast, the Proterozoic witnessed continuously decreasing crustal thickness, leaving the continents devoid of high mountains until the end of the eon. We link this gradually diminished orogenesis to the long-lived Nuna-Rodinia supercontinent, which altered the mantle thermal structure and weakened the continental lithosphere. This prolonged orogenic quiescence may have resulted in a persistent famine in the oceans and stalled life's evolution in Earth's middle age.

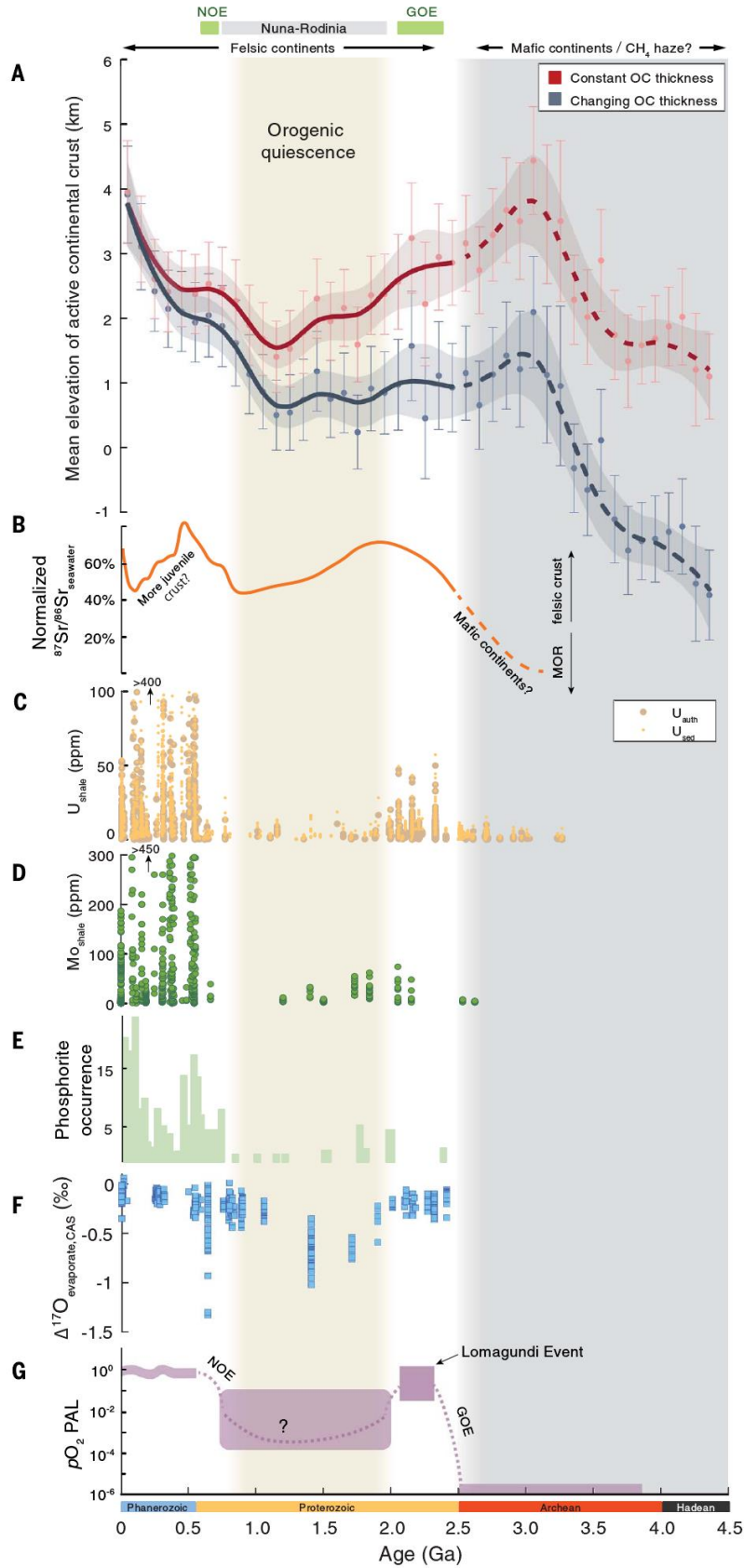


Figure 1. Elevation of the active continental crust over Earth’s history and evolution of Earth’s surface environment. (A) Elevation plotted as binned averages(bin size, 100 million years), with error bars

indicating ± 2 SEM. Also shown are the smoothed trends bracketed by 95% confidence intervals. The elevation of active continental crust can be calculated from our reconstructed crustal thickness using an isostasy model (10). We consider two end-member scenarios of oceanic crust thickness, one with constant thickness over time and the other decreasing thickness from the Hadean to the present day (10). (B) The normalized seawater Sr isotope curve is from (50), which removes the radiogenic decay effect and thus reflects the contributions from the mid-ocean ridge (MOR) and the felsic continental crust. The Sr isotope curve has decoupled from that of the elevation since ~ 450 Ma, which was probably caused by an increasing contribution from juvenile crust with MOR-like Sr isotopes (51). (C) Sediment U contents and authigenic U concentrations in black shales (42). (D) Mo concentrations in black shales (36). (E) Sedimentary phosphorite occurrence (39). (F) $\Delta^{17}\text{O}$ in evaporate and carbonate-associated sulfate (41). (G) Atmospheric O_2 partial pressure relative to present atmospheric level (PAL). The purple fields are from (52) and (53). The dashed curve in the Proterozoic field is our proposed path (schematic). NOE, Neoproterozoic Oxidation Event; GOE, Great Oxidation Event.

3. 俯冲带海洋磁异常的命运：一个全球性的评估

翻译人:李园洁 liyj3@sustech.edu.cn



Choe, H & Dymant, J. The fate of marine magnetic anomaly in subduction zones: A global appraisal. [J] Earth and Planetary Science Letters, 2021. 561, 116787.

<https://doi.org/10.1016/j.epsl.2021.116787>

摘要：海洋磁异常接近和进入俯冲带时会变弱和消失。之前的研究主要集中在日本海沟，结果表明俯冲之前，大洋岩石圈的挠曲产生正断层并恢复热液循环导致磁性矿物的蚀变；俯冲之后，俯冲板块的温度升高经过磁性矿物的居里温度时，热退磁会影响洋壳中的磁性矿物。目前没有其他俯冲带的研究。本文作者研究了五个俯冲带的磁异常演化过程。观测到的不同主要是由岩石圈年龄和相关的物理性质控制。俯冲之前，古老岩石圈的磁异常表现显著的与蚀变相关的衰减（20-30%），而 Cascadia 俯冲带的年轻岩石圈没有衰减，可能是 Juan de Fuca 板块几乎没有挠曲的原因。俯冲之后，俯冲板片的磁异常快速降低反映了喷出玄武岩的热退磁，在古老的岩石圈为 30%-40%，年轻岩石圈超过 70%。除了喷出玄武岩完全热退磁，老的岩石圈还保留有 40%的磁化强度，Cascadia 年轻岩石圈不到 30%。

ABSTRACT: Seafloor spreading magnetic anomalies of oceanic plates progressively decay and disappear when approaching and entering subduction. Previous studies focused on the Japan Trench showed that before subduction, the flexure of oceanic lithosphere opens normal faults and rejuvenates hydrothermal circulation which results in the alteration of magnetic minerals. After subduction, thermal demagnetization affects the magnetic minerals of the oceanic crust when the increasing temperature of the subducting slab passes their Curie temperature. No other subduction zone was investigated so far. Here we study the evolution of magnetic anomalies in five subduction zones. The major observed differences are controlled by the age of the lithosphere and related physical properties. Before subduction, magnetic anomalies of old oceanic lithosphere show a significant decay (20-30%) related to alteration whereas those of young lithosphere at the Cascadia subduction zone displays no such decay as a consequence of negligible flexure on the young Juan de Fuca plate. After subduction, the magnetic anomalies of the subducting plate show a rapid decay

reflecting the thermal demagnetization of extrusive basalt, amounting for 30-40% in old oceanic lithosphere and more than 70% in the young lithosphere of Cascadia. Beyond complete thermal demagnetization of extrusive basalt, about 40% of the magnetization remains in the old lithosphere and less than 30% in the young lithosphere of Cascadia.

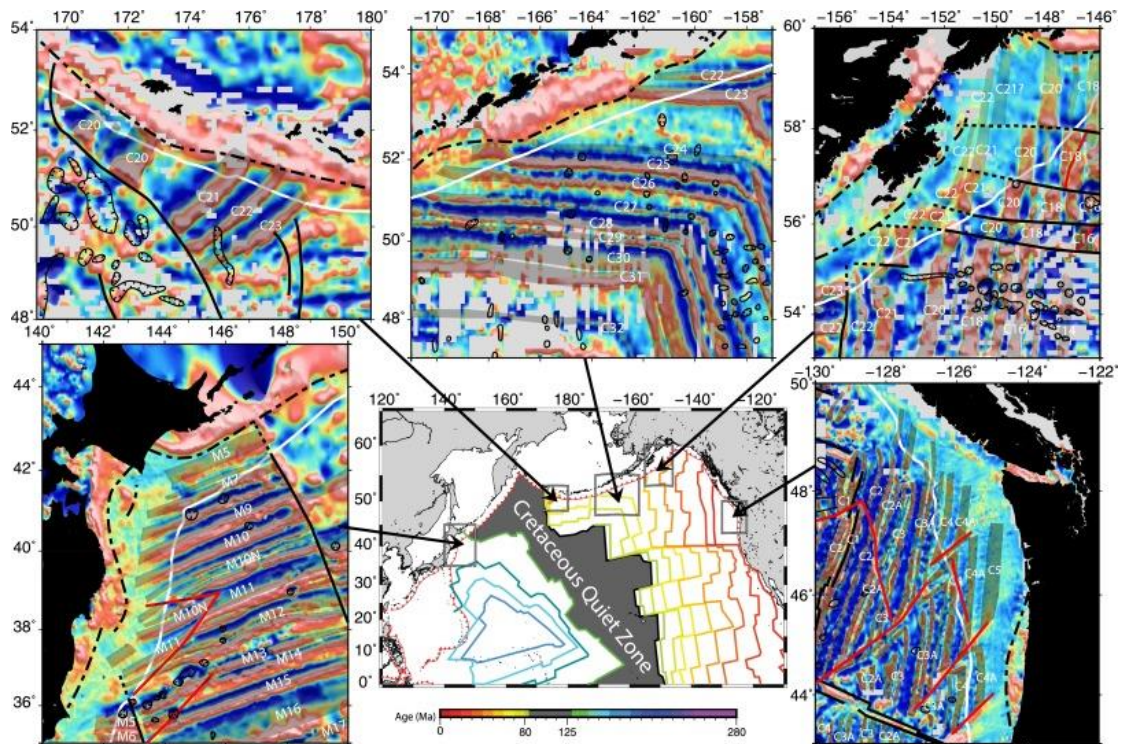


Figure 1. Five studied area where magnetic data are sufficiently dense to accurately constrain magnetic anomaly variations, excluding the Cretaceous Quiet Zone (CQZ). In the central bottom map, color lines display the age of oceanic lithosphere (after Müller et al., 2008) and boxes show the studied areas. In all other maps, colors represent the magnetic anomaly, black solid lines depict observed fracture zones and black dotted line fracture zones inferred from magnetic anomaly, red solid lines mark propagating rifts, white lines show the trench, and black dashed lines underline the induced magnetic anomalies from fore-arc mantle.

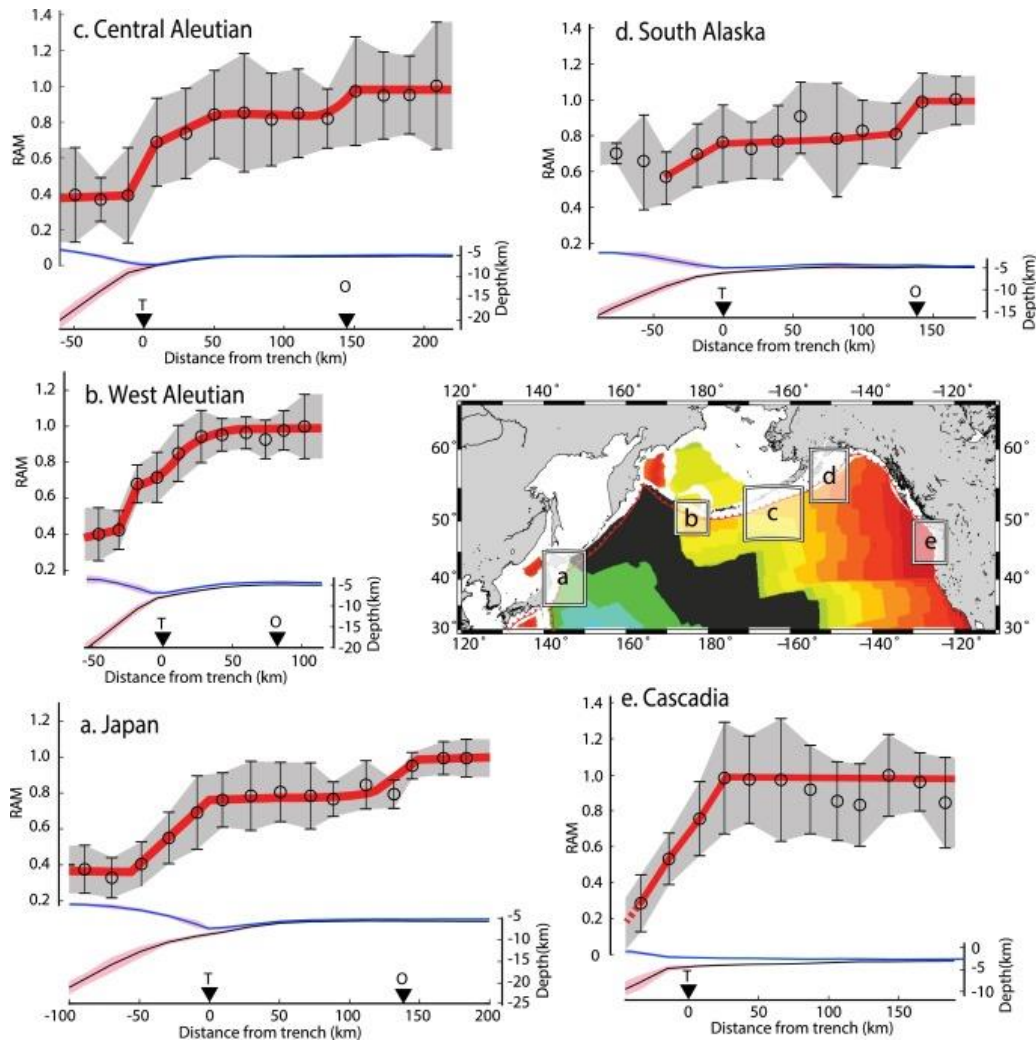


Figure 2. Remaining Amount of Magnetization (RAM) in subduction zones. In the right middle map, colors display the age of oceanic lithosphere (after Müller et al., 2008) and boxes show the studied areas. In all other graphs, the upper panel shows RAM variations across the subduction zone (circles, averaged value over 20 km with error bars, one standard deviation; thick red lines, interpreted trends, and grey area, uncertainty envelope), and the lower panel shows the bathymetry (blue line) and the basement geometry (black line; red area, uncertainty envelope). In graphs a, b, c and d, the RAM over mature oceanic lithosphere shows ~20% loss of amplitude between the outer rise and the trench due to rejuvenated hydrothermal circulation and the resulting alteration of magnetic minerals. After subduction, the RAM decreases rapidly, reflecting thermal demagnetization of the extrusive basalt and its magnetically soft titanomagnetite, until reaching ~40% - corresponding to the magnetization of the deeper crust and its magnetically harder magnetite. In graph e, the RAM over young oceanic lithosphere of the Cascadia subduction zone shows no decrease before subduction, and a rapid decrease just before

and after subduction, as a result of thermal demagnetization of the extrusive basalt layer related to the high heat flow and thermal blanketing from thick sediment layer.

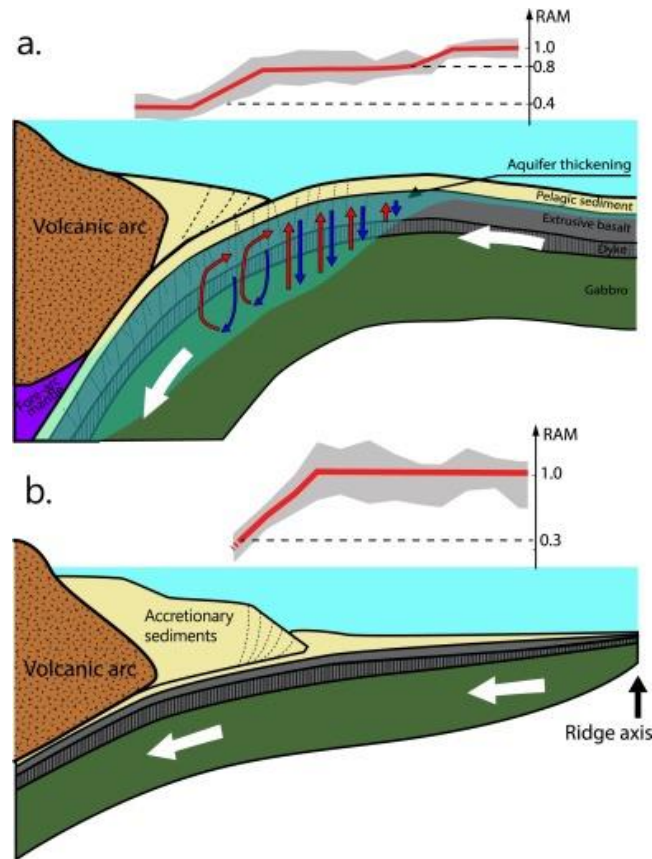


Figure 3. Magnetic signature of mature versus young subducting oceanic lithosphere. For each graph: Bottom, schematic illustration of the subduction zone (proportions are roughly correct horizontally but not vertically); Top, Remaining Amount of Magnetization. In the case of mature oceanic lithosphere, the RAM decreases by ~20% due to pervasive alteration of the magnetic mineral induced by hydrothermal circulation rejuvenated by the bending faults between the outer rise and the trench, and by an additional ~40% rapid decay due to the thermal demagnetization of titanomagnetite in the extrusive basalt induced by the increasing temperature and closed circulation of hot water after subduction, before stabilizing at ~40% corresponding to the contribution of magnetite in the deeper crust. In the case of young oceanic lithosphere, i.e. the Cascadia subduction zone, negligible flexure and thick pelagic sediments result in no decay in the outer-trench wall, but more than 70% of the magnetization is lost at and after subduction due to thermal blanketing of the hot young lithosphere by thick sediment deposits, the magnetization of the deeper crust amounting for less than 30%.

4. 地球化学差异反映的地幔深部不同的形成历史

翻译人：柳加波 liujb@sustech.edu.cn



Doucet L S, Li Z X, El Dien H G, et al. Distinct formation history for deep-mantle domains reflected in geochemical differences[J]. Nature Geoscience, 2020, 13(7): 511-515.

摘要：地球的地幔分为非洲和太平洋两大区域，由环太平洋俯冲带分隔开来，每个区域在下地幔中都有一个较大的低剪切波速度省（LLSVP）。然而，关于 LLSVP 是否随时间静止，还是动态地响应于整体俯冲形状的变化，这仍然存在争议。本文，我们收集了来自两个 LLSVP 之上的大洋岛屿和海洋高原的羽状玄武岩的放射同位素数据，这些玄武岩显示出两个地幔域的铅、钕和锶同位素组成不同。非洲地区在超大陆 Pangaea 的合并和破裂过程中显示出俯冲大陆物质的富集，而在太平洋地区则没有发现这种特征。这种深地幔地球化学二分法反映了 Rodinia 和 Pangea 超大陆周期中两个区域的不同演化历史，因此支持了板块构造与深地幔结构之间的动态关系。

ABSTRACT: The Earth's mantle is currently divided into the African and Pacific domains, separated by the circum-Pacific subduction girdle, and each domain features a large low shear-wave velocity province (LLSVP) in the lower mantle. However, it remains controversial as to whether the LLSVPs have been stationary through time or dynamic, changing in response to changes in global subduction geometry. Here we compile radiogenic isotope data on plume-induced basalts from ocean islands and oceanic plateaus above the two LLSVPs that show distinct lead, neodymium and strontium isotopic compositions for the two mantle domains. The African domain shows enrichment by subducted continental material during the assembly and breakup of the supercontinent Pangaea, whereas no such feature is found in the Pacific domain. This deep-mantle geochemical dichotomy reflects the different evolutionary histories of the two domains during the Rodinia and Pangaea supercontinent cycles and thus supports a dynamic relationship between plate tectonics and deep-mantle structures.

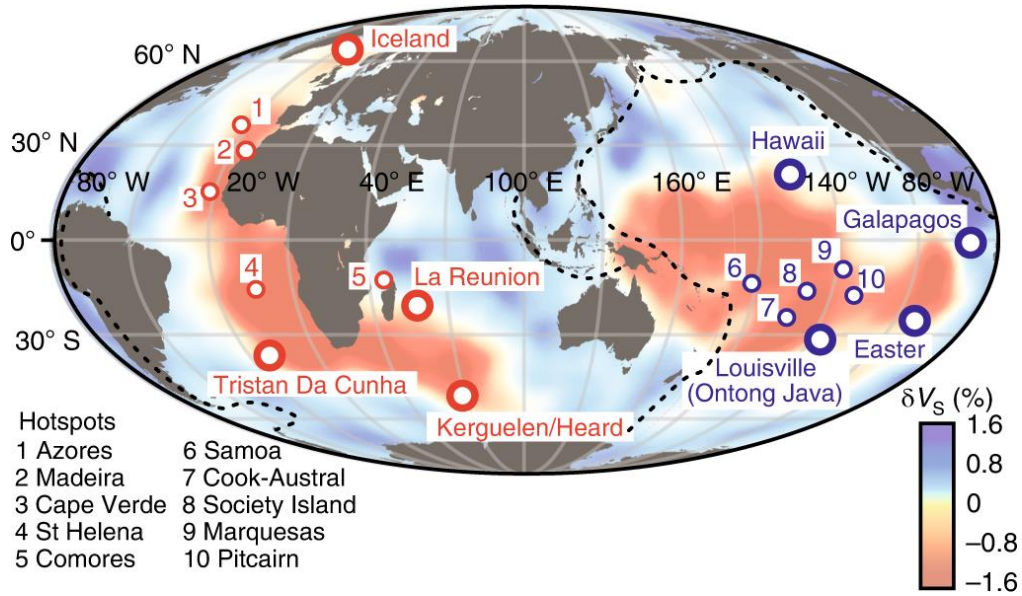


Figure 1: Global maps of the LLSVPs. Seismic shear-wave velocity anomalies (δV_s) are those of the mean S-wave tomography model s5mean. Also shown are the major OIBs and OPBs, with large circles denoting plumes of deep origin and small circles denoting plumes of shallower origin (Extended Data Fig. 3). The map is centred on the Equator and 100th meridian, and each meridian is separated by 30°.

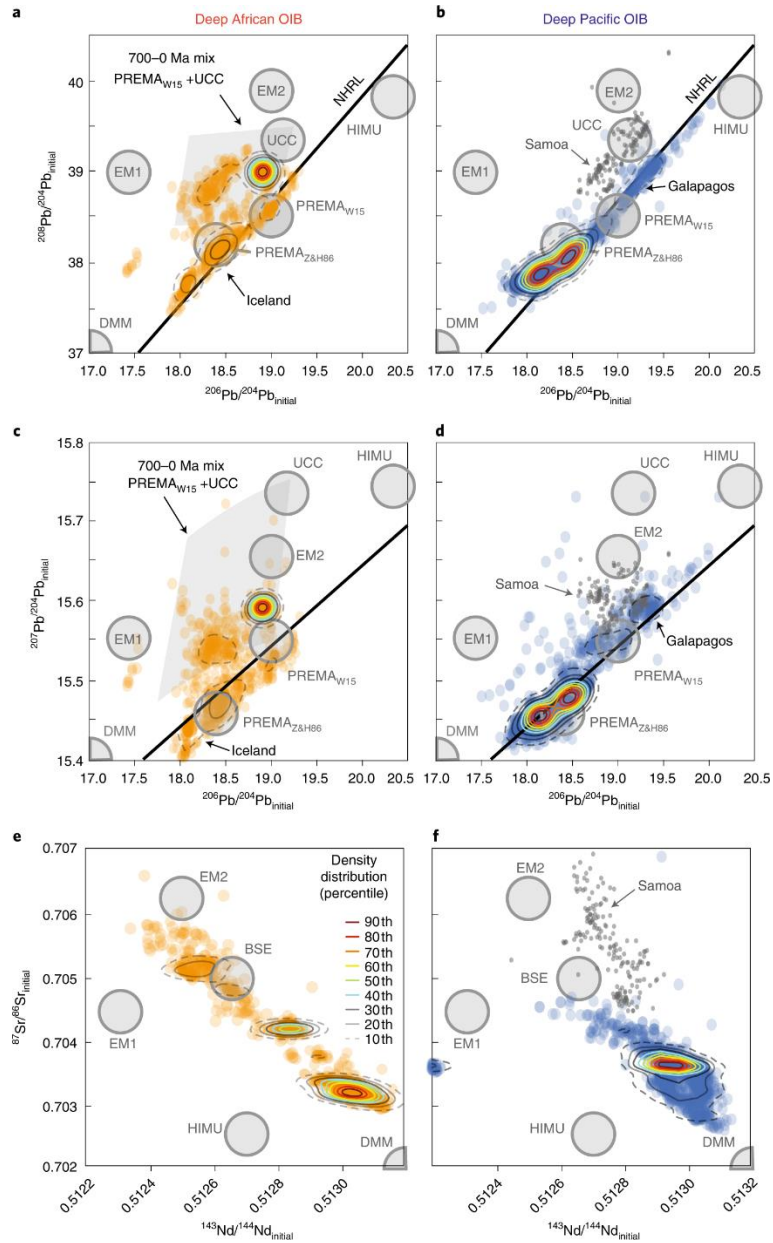


Figure 2: Isotopic data of OIBs and OPBs derived from the deep source of the African and the Pacific mantle domains. Isotopic compositions are back-calculated to initial compositions at the time of crystallization for Kerguelen and Ontong Java oceanic plateaus. a,b, $^{206}\text{Pb}/^{204}\text{Pb}$ versus $^{208}\text{Pb}/^{204}\text{Pb}$. c,d, $^{206}\text{Pb}/^{204}\text{Pb}$ versus $^{207}\text{Pb}/^{204}\text{Pb}$. e,f, $^{143}\text{Nd}/^{144}\text{Nd}$ versus $^{87}\text{Sr}/^{86}\text{Sr}$. The contour lines represent percentiles of the kernel density estimation (see Methods). Also shown are the NHRL that defines the DUPAL anomaly (above the NRHL), the prevalent mantle defined by Zindler and Hart (PREMAZ&H) and by White (PREMAW15), enriched mantle 1 (EM1), enriched mantle 2 (EM2), high- μ (HIMU) and the UCC isotopic endmembers. The grey fields shown in a and c are mixing modelling results of PREMAW15 + UCC between 700 and 0 Ma.

5. 不同风化程度好氧土壤对成土过程的磁响应



翻译人：张琪 zhangq7@sustech.edu.cn

Liu C C, Dupont-Nivet G, Wang W, Deng C L. *Magnetic response to pedogenesis in aerobic soils of different weathering degree [J]. Palaeogeography. Palaeoclimatology. Palaeoecology, 2021, 567, 110240.*

<https://doi.org/10.1016/j.palaeo.2021.110240>

摘要：磁学参数被广泛用于指示沉积记录中的古气候和古环境条件。然而，磁学参数与古气候之间的关系因风化程度不同而大相径庭。本文中通过对中国南方亚热带百色盆地的一个强烈风化红土剖面（大美遗址序列的不同风化强度层）的各种多学科参数进行研究，以了解好氧土壤中磁性矿物对成土作用的响应。我们发现，唯一与风化强度地球化学指标有很好相关性的常用环境磁学参数是 S-ratio（用于衡量高矫顽力组分与低矫顽力组分的相对含量）。HIRM(高矫顽力组分含量)和-IRM_{0.3T}(低矫顽力含量)是 S-ratio 的主要变量。磁性矿物分析表明，大美红土中 HIRM 和-IRM_{0.3T} 的主要载磁矿物分别是赤铁矿和磁赤铁矿。S-ratio、IRM_{0.3T} 与风化强度之间呈负相关，HIRM 与风化强度之间呈正相关，这与在这种强烈风化的情况下，磁赤铁矿向赤铁矿转化有利有关。如果能首先利用赤铁矿和铁磁性矿物的浓度关系来确定风化程度，那么将会更好的约束用磁学参数来解释环境问题。根据 HIRM 和-IRM_{0.3T} 之间线性相关的斜率，一种新的用于强烈风化红土的磁学风化指数被提出来。这些结果开启了利用环境磁学评估风化和古气候代用指标的应用。

ABSTRACT: Magnetic parameters are widely used to indicate paleoclimatic and paleoenvironmental conditions in sedimentary records. However, the relations between magnetic parameters and paleoclimate conditions are very different depending on the weathering degree. This study explores various multidisciplinary parameters across an intensely weathered red soil section in the Bose Basin (the Damei sequence with layers of different weathering intensity) of subtropical southern China to understand the magnetic mineral response to pedogenesis in aerobic soils. We find that the only commonly used environmental magnetic parameter that correlates well with

geochemical indices of weathering intensity, is the S-ratio (a measure of the relative amounts of high-coercivity remanence to low-coercivity remanence). HIRM (the absolute amount of high-coercivity remanence) and $-IRM_{0.3T}$ (the absolute amount of low-coercivity remanence) are the main variables in S-ratio. Mineral magnetic analyses indicate that the main carriers of HIRM and $-IRM_{0.3T}$ in the Damei red soils are respectively hematite and maghemite. Negative correlations between the S-ratio, the $IRM_{0.3T}$ and the weathering intensity, and a positive correlation between the HIRM and the weathering intensity relates to the transformation of pedogenic maghemite into hematite which is favored in such a case of intense weathering. It seems that environmental interpretations from magnetic parameters are better constrained if the weathering stage can be first determined using the relation between concentration of hematite and ferrimagnetic minerals. A new magnetic weathering index is proposed for intensely weathered red soils based on the slope of the linear correlation between HIRM and $-IRM_{0.3T}$. These results open applications for assessing weathering and pedoclimate proxies using environmental magnetism.

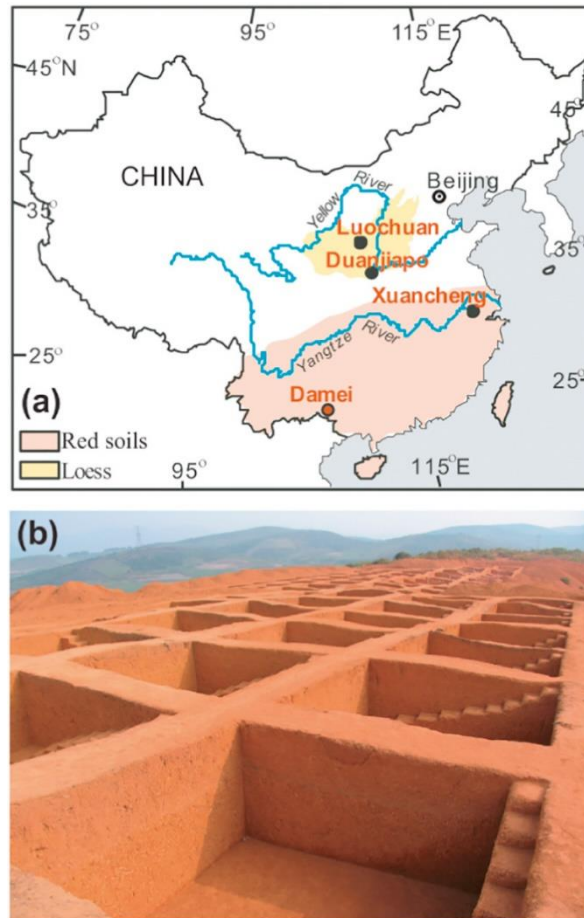


Figure 1. (a) Schematic map showing the distribution of red soils in southern China and loess in northern China and the Damei, Xuancheng, Luochuan and Duanjiapo sections investigated in this study (Bloemendal and Liu, 2005; Bloemendal et al., 2008; Liu et al., 2012; Liu et al., 2008a). The Yellow River and Yangtze River are the major river systems in north and south China, respectively. (b) Sampled section of the Damei site.

6. 晚中新世之前不能形成现代长江：来自碎屑白云母和钾长石 $^{40}\text{Ar}/^{39}\text{Ar}$ 年代学证据

翻译人：刘伟 inewway@163.com



Sun, X L, Tian Y T, Kuiper K F, et al. 2021. No Yangtze River Prior to the Late Miocene: Evidence from Detrital Muscovite and K-feldspar $^{40}\text{Ar}/^{39}\text{Ar}$ Geochronology. [J] Geophysical Research Letters.

<https://doi.org/10.1029/2020GL089903>

摘要：长江是亚洲最大的河流，一个多世纪以来，它的形成年龄和演变历史一直是争论的话题。在这里，我们对南京晚新生代河流砾石沉积中的碎屑白云母和钾长石进行 $^{40}\text{Ar}/^{39}\text{Ar}$ 测年，追踪晚新生代长江流域演化历史。研究发现，砾石沉积物中缺少长江上游的白云母和钾长石年龄信号，表明长江上游至少在晚中新世之前没有向长江下游提供沉积物。这些结果不支持长江在晚中新世之前的诞生。但支持另一种模式，其强调晚中新世之后长江上游融入中下游，形成目前的长江水系。

ABSTRACT: The Yangtze River is the largest river in Asia and its age and evolution has been the subject of debate for more than one century. Here, we applied a combination of detrital muscovite and K - feldspar $^{40}\text{Ar}/^{39}\text{Ar}$ dating on a set of samples from late Cenozoic Nanjing fluvial gravel sediments (overlain by basalt with ages of ~ 22.9 Ma and ~ 10.3 Ma) distributed along the lower Yangtze River to trace the late Cenozoic Yangtze drainage. It is found that the characteristic Cenozoic muscovite and K-feldspar age signals of the upper Yangtze are absent in the gravel sediments, indicating that the upper Yangtze did not supply sediment to the lower Yangtze before at least late Miocene time. These results do not support a pre-late Miocene birth of the Yangtze River, but favor an alternative model highlighting later integration of the upper Yangtze into the mid-lower reaches to form the current Yangtze drainage system.

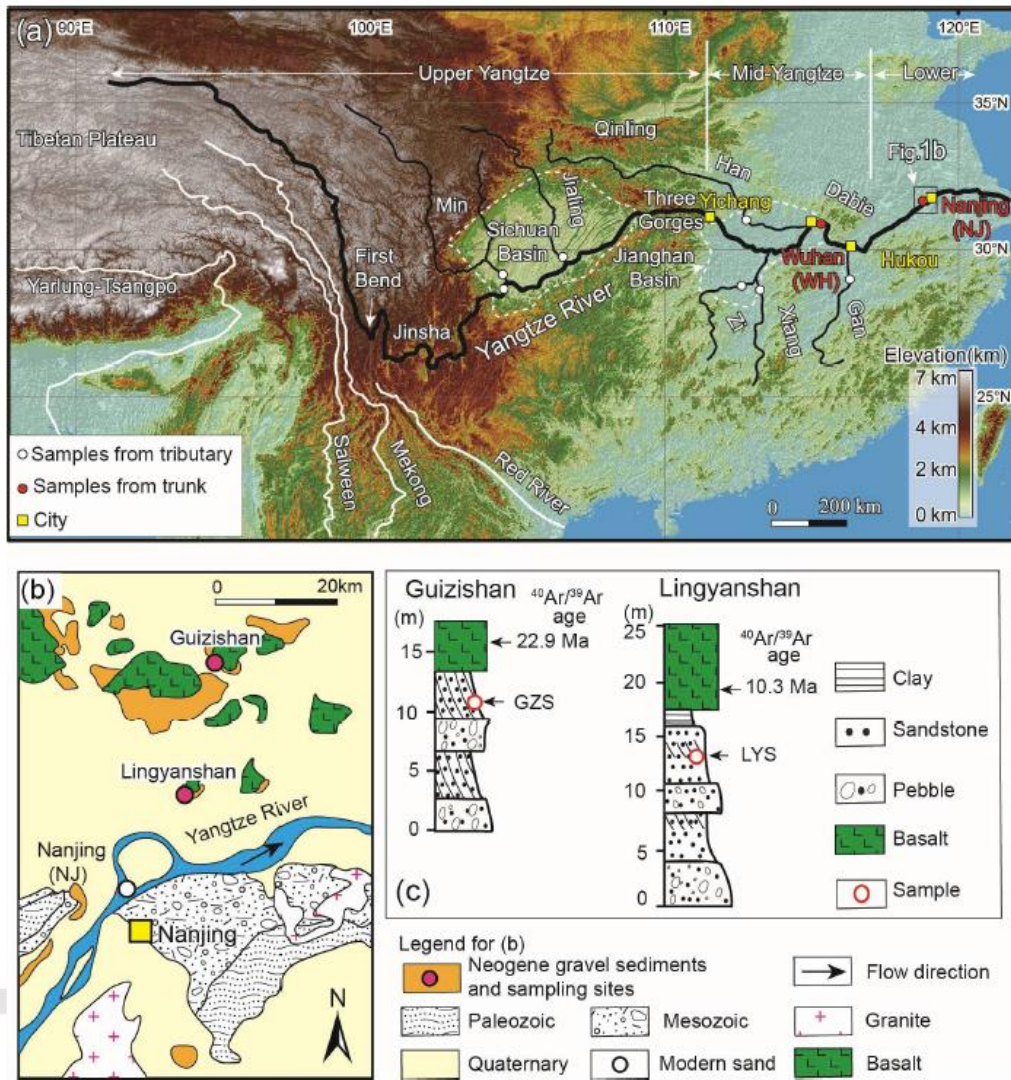


Figure 1. (a) Digital elevation model showing the major river systems in the east Asia. The thick black line represents the mainstream of the Yangtze River. Red circles denote the locations of the modern Yangtze trunk sand samples (WH and NJ), whereas those white circles represent modern sand samples from the major tributaries. (b) Generalized geological map of the study area. See figure 1a for tributary names and the location the panel b. NJ: sample location of modern sediment from the Yangtze River. (c) Lithological logs of the studied Nanjing gravel sediments. Basalts $^{40}\text{Ar}/^{39}\text{Ar}$ ages are from Zheng et al. (2013).

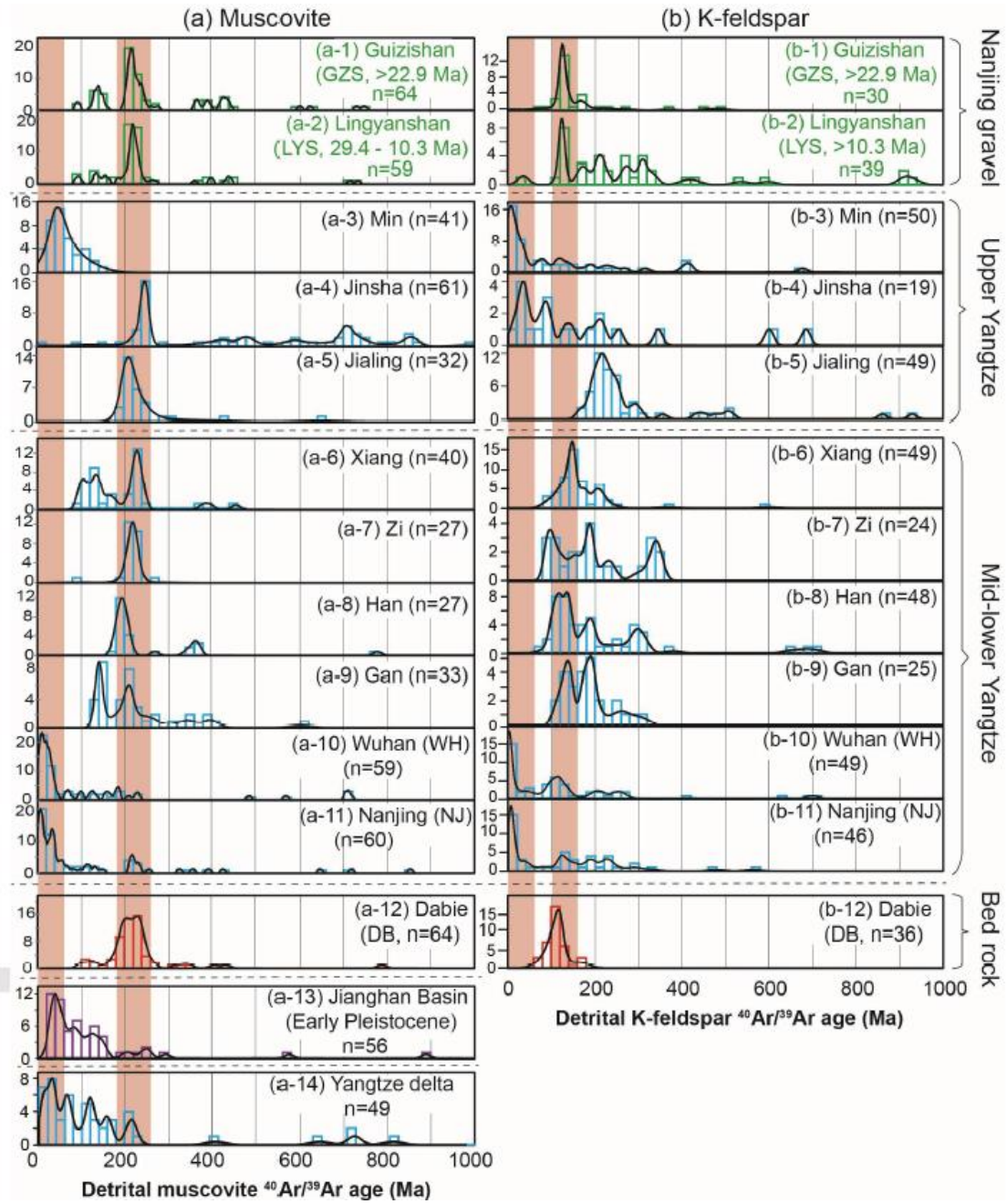


Figure 2. Comparison of muscovite (a) and K-feldspar (b) age distributions between Nanjing gravel sediments and potential source areas. Black lines are kernel density estimation (KDE). The detrital muscovite $^{40}\text{Ar}/^{39}\text{Ar}$ ages of the major tributaries (Jinsha, Min, Jialing, Xiang, Han, Zi and Gan) (panel a-3-9) and Jiangnan Basin (panel a-13) are from the Sun et al., (2016, 2018), and the Yangtze delta muscovite (panel a-14) from Hoang et al. (2010), whereas others are newly derived. Bedrock muscovite and k-feldspar $^{40}\text{Ar}/^{39}\text{Ar}$ ages for the Dabie orogen are compiled from Hacker et al., (2000), Liu et al., (2008), Ratschbacher et al., (2000, 2003), Xu et., (2000, 2010) and references therein.

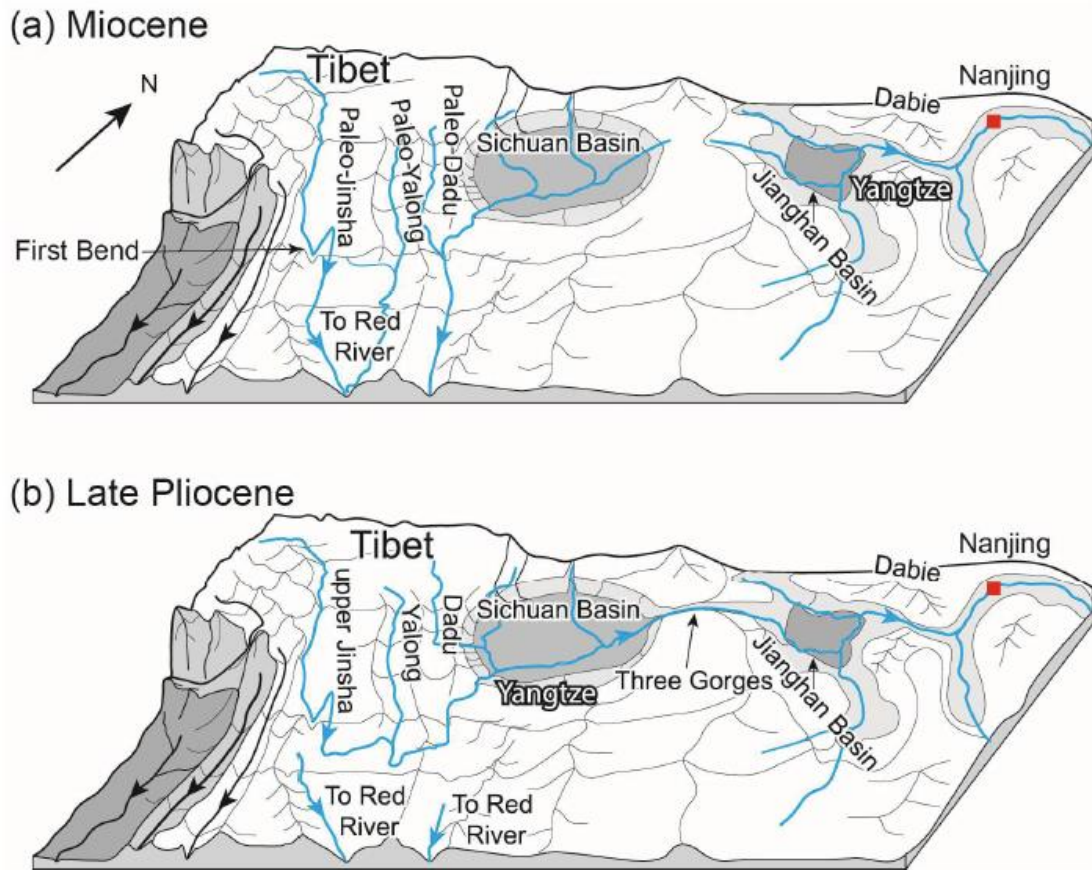


Figure 3. Schematics showing the drainage system and evolution of the Yangtze River. At Miocene time (a), drainages which are now the upper Yangtze did not provide sediments to the lower reaches (as shown by our new results), and possibly flowed south into the Red River. (b) The capture of the upper Yangtze by mid-lower reaches occurred at some time between the late Miocene and Pliocene. Blue and black arrows indicate flow river directions.

7. 中国黄土高原陆生蜗牛壳体耦合同位素与稳定同位素的气候指示

翻译人：杨会会 11849590@mail.sustech.edu.cn



Dong J B, Eiler J, An Z S et al. *Clumped and stable isotopes of land snail shells on the Chinese Loess Plateau T and their climatic implications*[J]. *Chemical Geology*, 2020, 533,119414.

<https://doi.org/10.1016/j.chemgeo.2019.119414>

摘要： 我们报道了中国黄土高原中部和南部的洛川与渭南剖面的现代及末次冰期的蜗牛壳体碳酸盐的稳定同位素组成结果 ($\delta^{13}\text{C}_{\text{shell}}$, $\delta^{18}\text{O}_{\text{shell}}$) 与耦合同位素组成结果 (Δ_{47})。我们的研究揭示出现代蜗牛平均 Δ_{47} 温度 (T_{47}) 和研究区蜗牛生长季的监测温度相一致，且比冰期蜗牛化石的结果要高 $\sim 10^\circ\text{C}$ 。此外，现代蜗牛壳体的平均 $^{13}\text{C}_{\text{shell}}$ 是比蜗牛化石结果更亏损的。我们推测 $^{13}\text{C}_{\text{shell}}$ 不能记录中国黄土高原地区植被群落的变化 (如 C3/C4 比值)，而可能主要表达的是干旱条件下亏损值反映了降低的干燥度。而且，现代蜗牛重建的肉体水分 $\delta^{18}\text{O}_{\text{water}}$ 是现代生长季降水 $\delta^{18}\text{O}$ 和化石蜗牛的 $\delta^{18}\text{O}_{\text{water}}$ 要偏富的。这一对比结果可能和温暖条件下现代蜗牛体内/摄入的环境水 ^{18}O 的高度蒸发富集相关。因此，我们认为直接用 $\delta^{18}\text{O}_{\text{shell}}$ 重建降水氧同位素是很难的，更高的 $\delta^{18}\text{O}_{\text{shell}}$ 和 $\delta^{18}\text{O}_{\text{water}}$ 值可能指示的是中国黄土高原地区冰期-间冰期尺度更高的环境温度或者更强的蒸发富集。

Abstract: We report stable ($\delta^{13}\text{C}_{\text{shell}}$, $\delta^{18}\text{O}_{\text{shell}}$) and clumped isotope (Δ_{47}) compositions of modern and last glacial fossil snail shell carbonates from the Luochuan and Weinan sections on the central and southern Chinese Loess Plateau (CLP). Our study reveals that the average Δ_{47} temperature (T_{47}) of modern snails is consistent with monitored temperatures during the snail growing season at the studied locations and is $\sim 10^\circ\text{C}$ higher than that of fossil snails from glacial time. Moreover, the average $\delta^{13}\text{C}_{\text{shell}}$ of modern snails is more depleted than that of fossils. We argue that the $\delta^{13}\text{C}_{\text{shell}}$ cannot record changes in plant communities (i.e., the C3/C4 ratio) on the CLP and may mainly indicate arid conditions with depleted values reflecting reduced aridity. Additionally, the reconstructed snail body water $\delta^{18}\text{O}$ ($\delta^{18}\text{O}_{\text{water}}$) of modern snails is more enriched than $\delta^{18}\text{O}$ in

modern growing season precipitation and $\delta^{18}\text{O}_{\text{water}}$ of fossils. This contrast may be related to the high degree of evaporative enrichment of environmental water ^{18}O in the body/ingested by modern snails under warm conditions. Therefore, we suggest that using $\delta^{18}\text{O}_{\text{shell}}$ to directly reconstruct the oxygen isotopes of precipitation is difficult and that higher $\delta^{18}\text{O}_{\text{shell}}$ and $\delta^{18}\text{O}_{\text{water}}$ values probably indicate higher environmental temperature/stronger evaporative enrichment on glacial-interglacial timescales on the CLP.

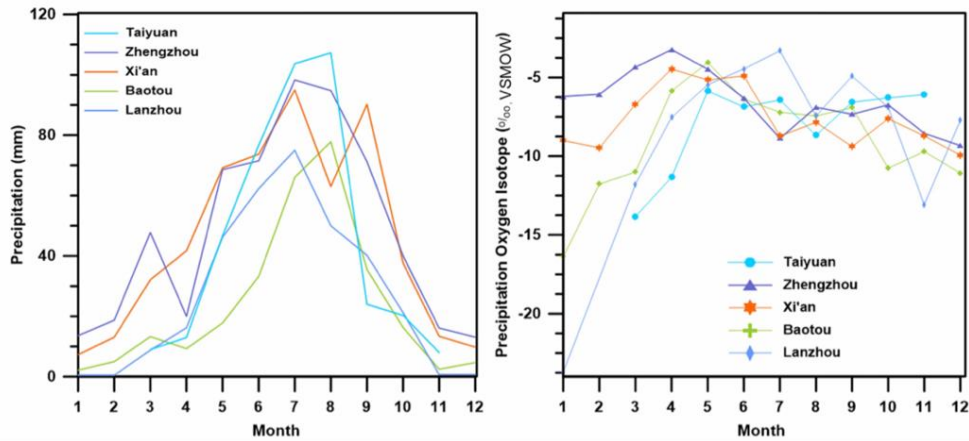


Figure 1. The monthly mean precipitation (left, data from <http://data.cma.cn/>) and precipitation isotopes (right, data from <http://isohis.iaea.org>) at sites on/around the CLP. Precipitation is mainly concentrated from April to October, and the corresponding precipitation $\delta^{18}\text{O}$ mainly varies between -4‰ and -9‰ .

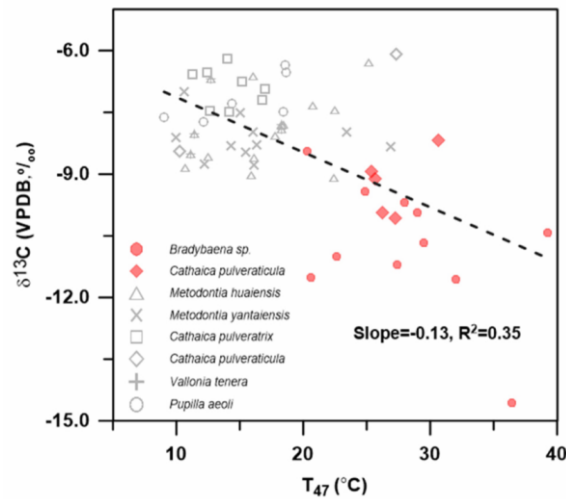


Figure 2. Correlation between $\delta^{13}\text{C}$ and T_{47} for fossil and modern snail shells. Different species are shown by different symbols, and modern snails are shown by red filled symbols. (For interpretation of the references to color in this figure legend, the reader is referred to the web version of this article.)

8. 全新世时期海洋驱动和地形控制的非线性冰川撤退：位于南极 Ross Sea 西南部



翻译人：王浩森 11930841@mail.sustech.edu.cn

Jones R S, Gudmundsson G H, Mackintosh A N, et al. Ocean-driven and topography-controlled nonlinear glacier retreat during the Holocene: southwestern Ross Sea. [J], Antarctica. Geophysical Research Letters, n/a: e2020GL091454.

<https://doi.org/10.1029/2020GL091454>

摘要：最近南极洲冰盖量的损失被归咎于温暖的海水的涌入，这促使接地线后退和冰层变薄。在全新世时期，Ross Sea 西南部也发生了周期性的后退和快速变薄，而今该海域容纳了寒冷的海水。我们利用有限元冰流模型研究了海温和地形在该地区冰消过程中的角色。首先，我们的实验表明，海底地形控制着接地线后退的空间模式。地形中固定点限制了冰流失的速度，直到后退距离超过测深阈值为止。其次，海洋的热变化决定了这种冰消的时间。在全新世早期到中期，海冰融化的加快指示着间冰期记录，这可能表明该地区曾经存在过温暖的海水。因此在几个百年的尺度上，虽受地形控制，冰块质量损失的非线性速率主要受海温的驱动。

ABSTRACT: Recent ice sheet mass loss in Antarctica has been attributed to an influx of warm ocean waters, which drove grounding - line retreat and ice thinning. Episodic retreat and rapid thinning also occurred in the southwestern Ross Sea during the Holocene, which today accommodates cold ocean waters. We applied finite - element ice - flow modeling to investigate the roles of ocean temperature and bed topography in the deglaciation of this region. First, our experiments demonstrate that bed topography controlled the spatial pattern of grounding - line retreat. Topographic pinning points limited the rate of ice loss until retreat progressed beyond a bathymetric threshold. Second, ocean thermal forcing determined the timing of this ice loss. Enhanced ocean - driven melt is required during the Early - to - Mid Holocene to replicate geological records of deglaciation, possibly indicating that warm ocean waters were once present in this region. On multi - centennial timescales, ocean temperature drove, while bed topography controlled, nonlinear rates of ice mass loss.

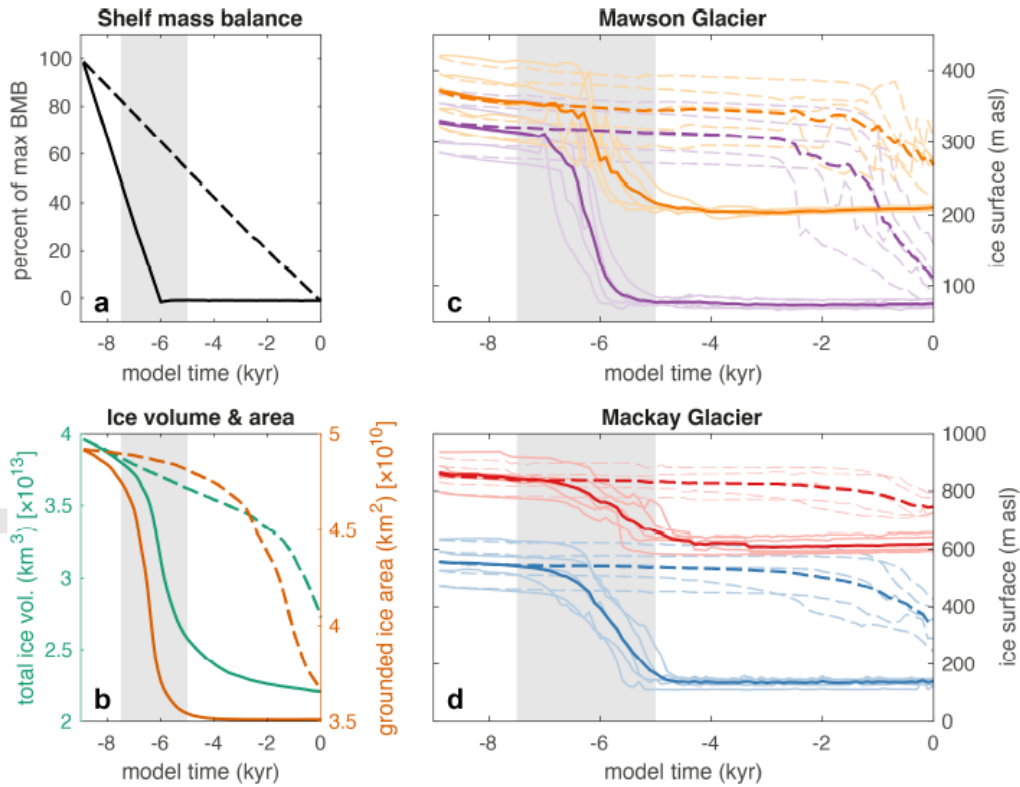


Figure 1. a) Basal mass balance (BMB) forcing in experiments E1 (dashed line) and E2 (solid line), with the resulting simulated changes in ice volume and grounded ice area (b), and corresponding changes in ice surface elevation at Mawson Glacier (c) and Mackay Glacier (d). The sites of Mt Murray, Bruce Point, Gondola Ridge and Low Ridge are colored orange, purple, red and blue, respectively. The bold lines represent the mean of the individual simulations in each experiment, while the period of observed rapid thinning (7.5–5 kyr ago) is highlighted as a grey area. Accelerated ice loss occurs in both E1 and E2, however, only E2 replicates the timing recorded by the geological data.

9. 利用岩石磁学对青铜时代 Ada Tepe 金矿场（保加利亚）的考古材料进行识别和分类



翻译人：曹伟 11930854@qq.com

Jordanova N, Jordanova D, Tcherkezova E, et al. Identification and Classification of Archeological Materials From Bronze Age Gold Mining Site Ada Tepe (Bulgaria) Using Rock Magnetism[J]. Geochemistry, Geophysics, Geosystems, 2020, 21(12).

<https://doi.org/10.1029/2020GC009374>

摘要：欧洲最古老的露天金矿的考古材料已经通过岩石磁学方法进行调查，这也是该遗址多学科研究的一部分。本项研究的目的是利用岩石的磁性特征（磁化率、非磁滞剩磁、等温剩磁和不同的磁性颗粒比值参数）对收集的 177 个样品进行分类，这些样品取自青铜时代晚期的废物堆、原始岩石，天然土壤和栽培层土壤。要素和聚类分析表明，四类分组对磁学矿物数据解释效果最好。温度磁学性质和热退磁结果表明，样品中的磁学矿物主要包括磁铁矿/磁赤铁矿、赤铁矿和针铁矿。根据样品的磁性特征，分别确定了 1 组和 3 组样品是受到用火建筑和火堆遗址的影响。2 组样品以针铁矿和赤铁矿为主，因此确定为岩石残留物。4 组中的材料显示出天然土壤的典型磁性特征，因此其与这类材料有关。所获得的样本分类结果与考古学研究结果吻合良好。遗址中各组分的空间分布为采矿活动的位置、纵向分布和所用技术提供了有价值的环境信息。结果表明，磁性矿物分析是一种准确、灵敏、高效的古采矿材料表征和分类方法。

ABSTRACT: Archeological materials from the most ancient open-pit gold mine in Europe have been investigated using mineral magnetic methods as part of the multidisciplinary research of the site. The aim of the study was to employ rock-magnetic characteristics (magnetic susceptibility, anhysteretic remanent magnetization, isothermal remanent magnetization and various magnetic grain-size dependent ratios) for classification of a collection of 177 samples, taken from Late Bronze age waste heaps, pristine rocks, natural soils and soils from cultural layers. Factor analysis and k-

means cluster analysis revealed that four clusters explain the best mineral magnetic data. Results from the thermomagnetic analysis and thermal demagnetization of composite isothermal remanence proved that the main magnetic minerals in the collection are magnetite/maghemite, hematite, and goethite. Based on the magnetic properties, samples from clusters 1 and 3 were identified as influenced by fire-archaeological structures and waste heaps with the use of fire setting, respectively. Samples belonging to cluster 2 were dominated by goethite and hematite, thus identified as rock residues. Materials grouped in cluster 4 showed magnetic characteristics typical of natural soils and were thus related to this class of materials. The obtained clustering of the samples agreed well with their archeological assignment. Spatial distribution of cluster members across the site provides valuable environmental information for the location of the mining activities, their lateral spread and the technology used. It was concluded that magnetic mineral analysis is a precise, sensitive, and a highly effective method for characterization and classification of materials from ancient mining.

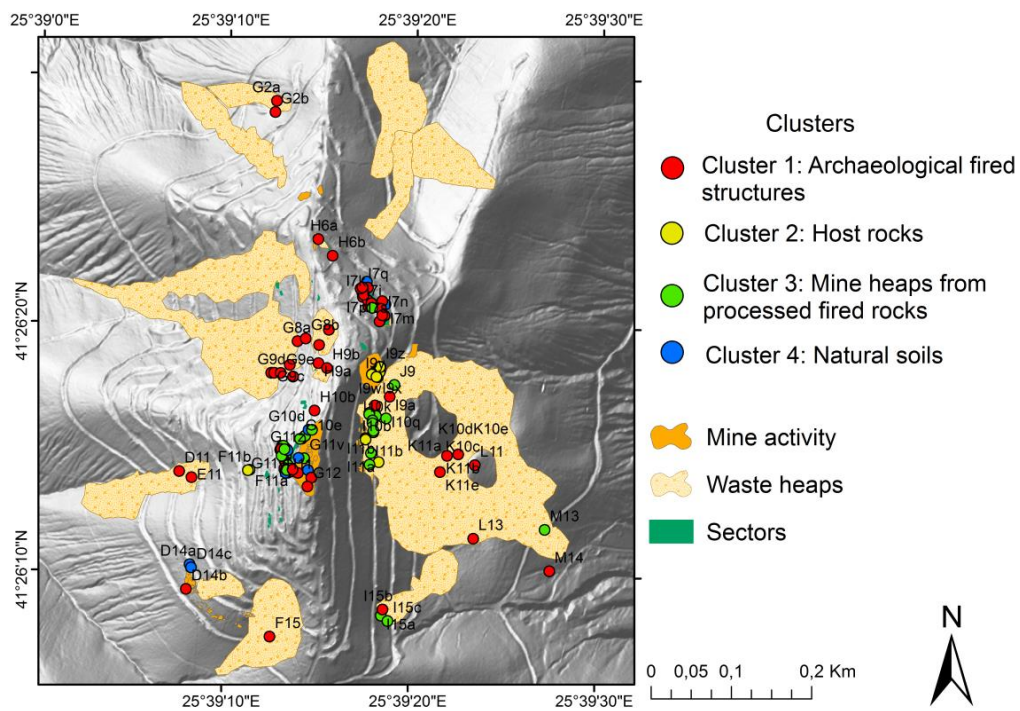


Figure 1. Spatial distribution of samples separated in the four clusters.

10. 冰消期西南太平洋深海通风变化

翻译人：张亚南 zhangyn3@mail.sustech.edu.cn



Dai Y H, Yu J M, Patrick A R. *Deglacial Ventilation Changes in the Deep Southwest Pacific [J]. Paleoceanography and Paleoclimatology*, 2021,36(2), e2020PA004172.

<https://doi.org/10.1029/2020PA004172>

摘要：海洋碳储库在末次冰盛期（LGM）和随后的冰消期期间的变化过程目前还尚不完全清楚。我们。本文在南大洋（太平洋扇区）现代下环极深水（LCDW）深度的位置提出了一个新的高分辨率的放射性碳重建结果（ $\delta^{14}\text{R}$ ）。我们的结果表明 $\delta^{14}\text{R}$ 在 H1 和新仙女木时期（YD）有所增加，这与 H1 和 YD 时期南大洋老碳从深部-浅部的转移相一致。结果还表明在南极的冷逆转期间（Antarctic Cold Reversal） $\delta^{14}\text{R}$ 首次明显下降了 80%左右，指示了西南太平洋深水通风条件变弱。与南大洋海冰的增加和 UCDW 与 LCDW 分层加剧相一致。ACR 期间海水分层的增强可能促进了海洋碳储库的增加，有效地限制了海洋对 CO_2 的释放，使得该时期冰心记录到的 CO_2 水平较为稳定。

ABSTRACT: Processes underlying changes in the oceanic carbon storage during the Last Glacial Maximum and the subsequent deglaciation are not fully understood. Here, we present a new high-resolution radiocarbon reconstruction (expressed as $\delta^{14}\text{R}$) at the depth of the modern Lower Circumpolar Deep Water from the Pacific Sector of the Southern Ocean. Our record shows $\delta^{14}\text{R}$ increases during Heinrich Stadial 1 and the Younger Dryas that agree with the deep-to-shallow transfer of old carbon in the Southern Ocean during these two periods. Our record also shows, for the first time, a clear $\sim 80\%$ decline in $\delta^{14}\text{R}$ during the Antarctic Cold Reversal (ACR), indicating the development of poorly ventilated conditions in the deep Southwest Pacific. These conditions are consistent with the increased Southern Ocean sea-ice and associated stratification between Upper and Lower Circumpolar Deep Waters. This enhanced stratification in the deep South Pacific possibly facilitated greater carbon storage in the ocean interior during the ACR, effectively limiting oceanic CO_2 release and contributing to the atmospheric CO_2 plateau as observed in ice cores at that time.

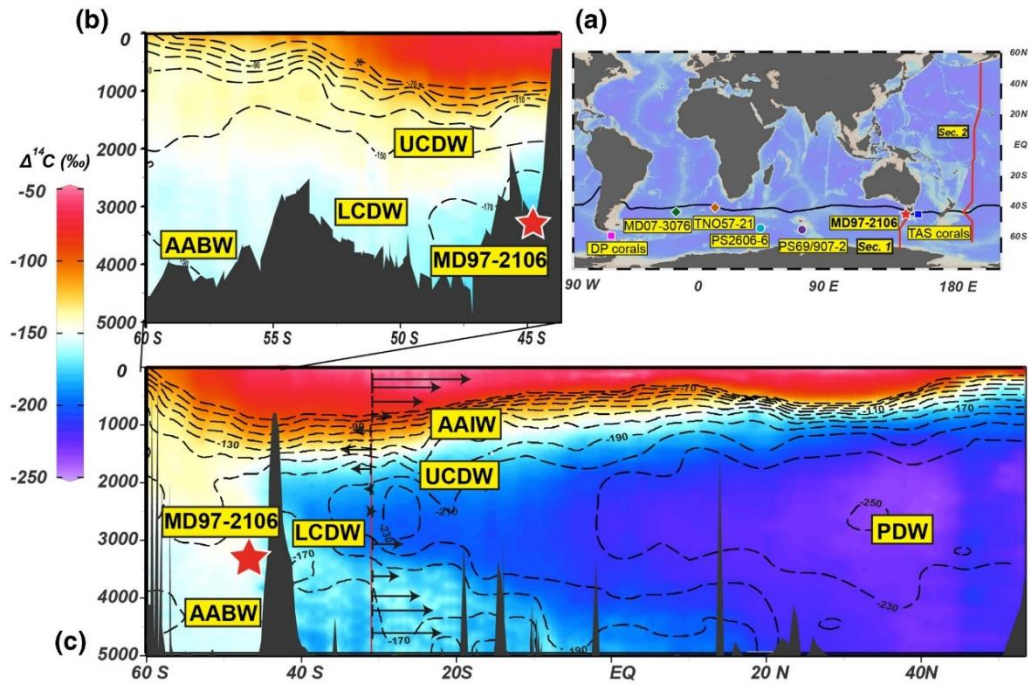


Figure 1. (a) Location of core MD97-2106, and other records discussed in the paper. The black curve represents the annual mean position of the modern STF. (b) Natural seawater $\Delta^{14}\text{C}$ transect along sections 1 shown in (a). (c) The same as (b) but for section 2 (Key et al., 2004). Black arrows in (c) indicate modern water transport across 32°S in the Pacific (Ganachaud, 2003). STF, Subtropical Front. AABW, Antarctic Bottom Water; LCDW, Lower Circumpolar Deep Water; UCDW, Upper Circumpolar Deep Water; AAIW, Antarctic Intermediate Water; PDW, Pacific Deep Water.

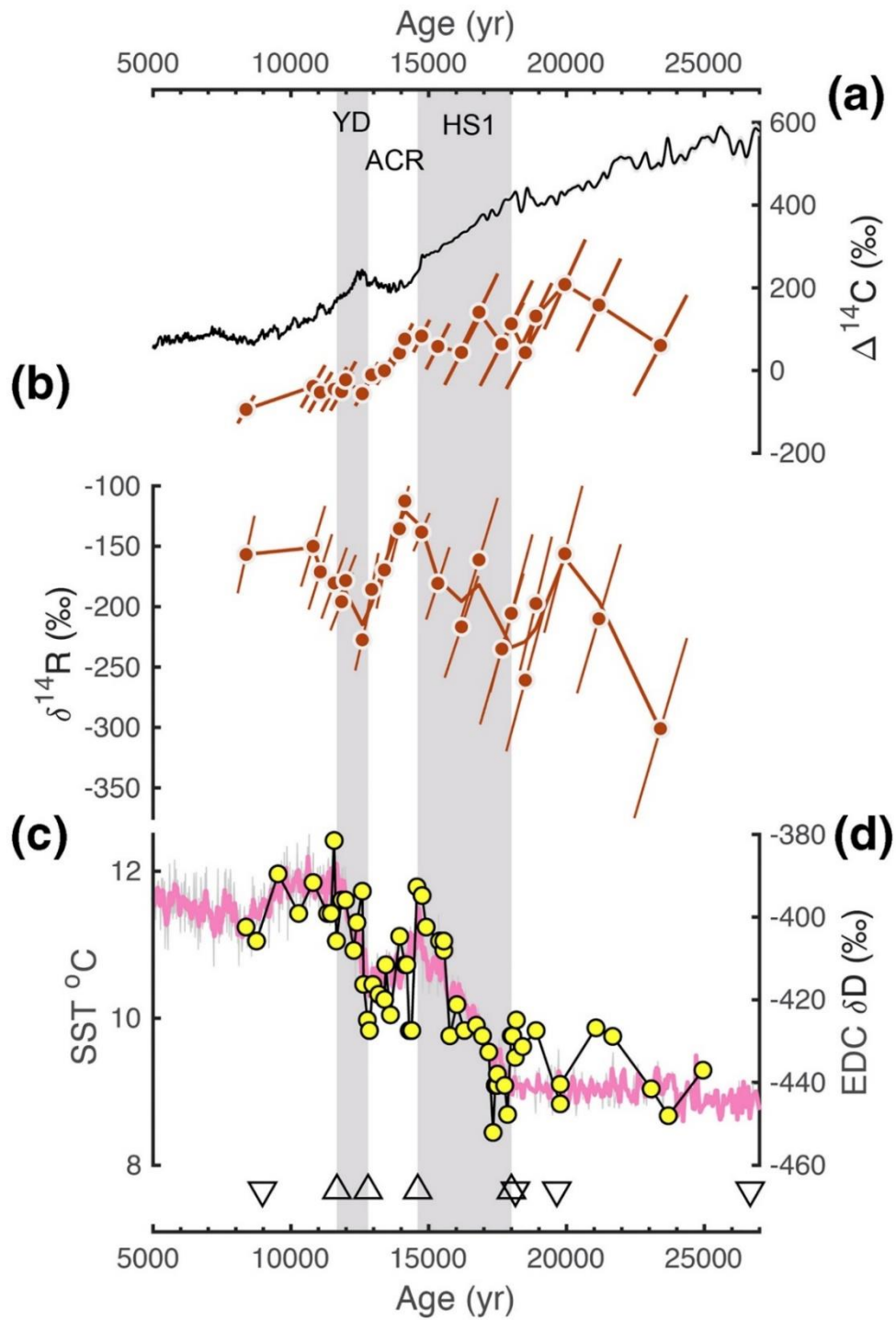


Figure 2. (a) MD97-2106 benthic $\Delta^{14}\text{C}$ with $\pm 1\sigma$ uncertainties compared to IntCal20 atmospheric $\Delta^{14}\text{C}$ (Reimer et al., 2020). (b) MD97-2106 $\delta^{14}\text{R}$. (c) MD97-2106 SST reconstruction based on *G. bulloides* Mg/Ca. (d) EDC δD (Jouzel et al., 2007). Upward and downward triangles represent age control points based on SST- δD alignment and planktic radiocarbon dates, respectively. Gray bars indicate the YD and HS1. SST, sea surface temperature. EDC, EPICA Dome C; YD, Younger Dryas; HS, Heinrich Stadial 1.

11. 目前大西洋经向翻转环流是近千年来最弱的

翻译人: 张伟杰 12031188@mail.sustech.edu.cn



Caesar L, McCarthy G D, Thornalley D J R, et al. *Current Atlantic Meridional Overturning Circulation weakest in last millennium. [J] Nature Geoscience. 2021.*

<https://doi.org/10.1038/s41561-021-00699-z>

摘要: 大西洋经向翻转环流(AMOC)是地球上主要的海洋环流系统之一,它重新分配了地球上的热量,并对气候产生了重大影响。在这里,我们比较了各种公布的代用指标记录,以重建大约公元400年以来AMOC的演变。现在出现了一幅相当一致的AMOC图景:在经历了一段长而相对稳定的时期后,从19世纪开始出现了最初的弱化,然后在20世纪中叶出现了第二次更迅速的衰退,导致了近几十年AMOC的最弱状态。

ABSTRACT: The Atlantic Meridional Overturning Circulation (AMOC)—one of Earth’s major ocean circulation systems—redistributes heat on our planet and has a major impact on climate. Here, we compare a variety of published proxy records to reconstruct the evolution of the AMOC since about ad 400. A fairly consistent picture of the AMOC emerges: after a long and relatively stable period, there was an initial weakening starting in the nineteenth century, followed by a second, more rapid, decline in the mid-twentieth century, leading to the weakest state of the AMOC occurring in recent decades.

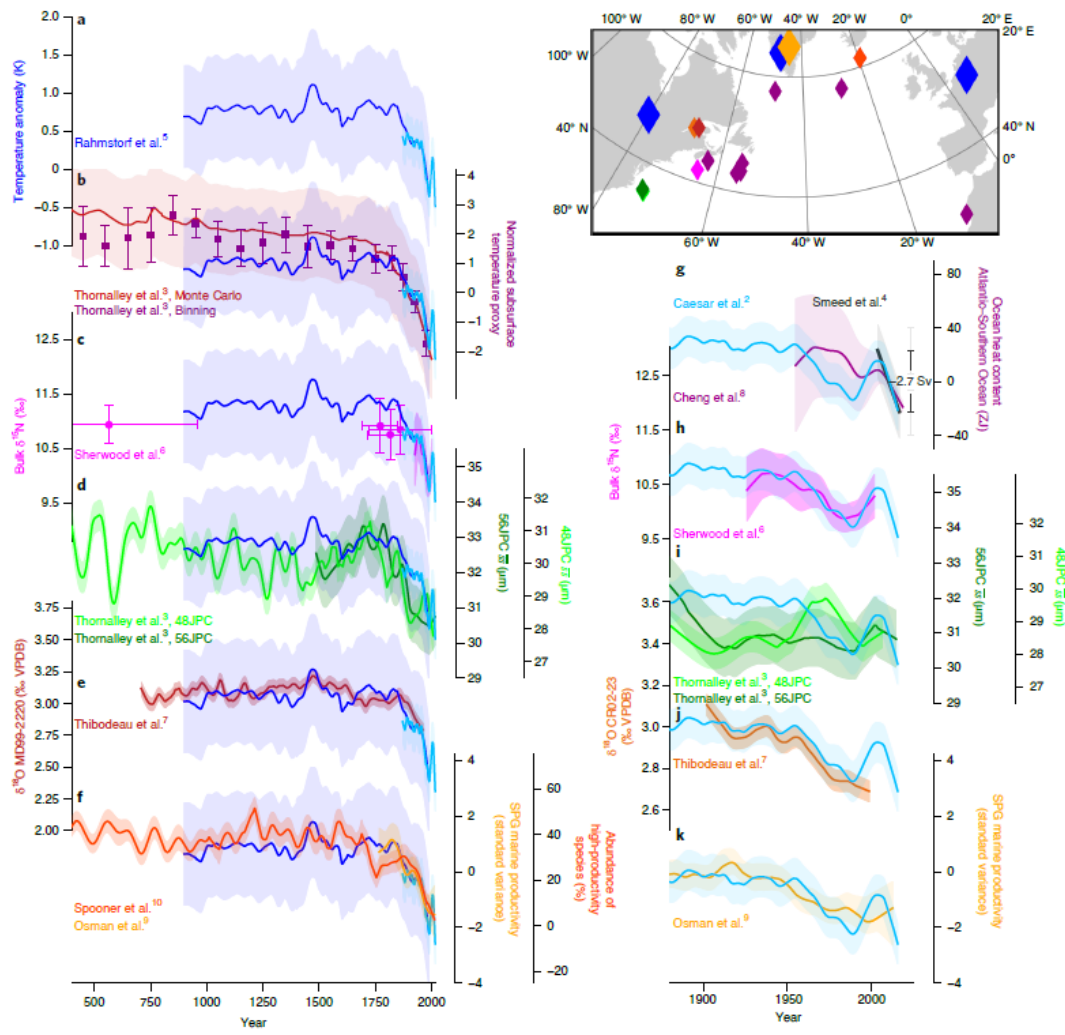


Figure 1. SST-based AMOC reconstructions compared with various proxy reconstructions. a, The SST-based proxies (light and dark blue) represent the North Atlantic temperature response to changes in the Atlantic meridional heat transport associated with an AMOC slowdown. b–k, It is compared with proxy records of subsurface ocean temperatures (purple) (b), $\delta^{15}\text{N}$ data of deep-sea gorgonian corals (magenta) (c,h), mean grain size of sortable-silt data ss (shades of green, shown with a 12-year lag to the temperature-based indices) (d,i), $\delta^{18}\text{O}$ data in benthic foraminifera (shades of brown) (e,j), the relative abundance of *T. quinqueloba* in marine sediment cores (orange-red) (f), methanesulfonic acid concentration in Greenland ice cores (orange) (f,k), both indicators for local/regional marine productivity, and the relative change in Atlantic Ocean heat content versus that in the Southern Ocean (dark magenta) (g). As a reference for the actual change in volume transport, the April 2004–April 2018 linear trend of the RAPID data4 (black) is given (g). The map (using the same colour-coding as the time series) gives an overview of the various locations the

proxies were taken from (with small markers denoting single sites and large markers denoting the areas with multiple proxy sites). All curves were smoothed with a 20-year (50-year) LOWESS filter for the shorter (longer) time series to make them more comparable. Shading and error bars show the 2σ (95%) confidence intervals of the individual proxies as they were reported and the uncertainty of the AMOC representation of the Caesar et al. (2018) temperature proxy, respectively (Methods). SPG, subpolar gyre; VPDB, Vienna PeeDee Belemnite; ZJ, zetajoules.

12. 硼同位素约束 800 kyr 以来的东亚季风变化

翻译人: 李海 12031330@mail.sustech.edu.cn



Lei F, Wei H Z, Yi S W, et al. 2021. Variations of the East Asian monsoon over the past 800 kyr constrained by the boron isotope composition of paleo-rainwater inferred from loess-paleosol deposits in NE China. [J] *Earth and Planetary Science Letters*, 561: 116826.
<https://doi.org/10.1016/j.epsl.2021.116826>

摘要: 对牛羊子沟的黄土-古土壤序列的硼同位素进行研究, 首次使用古雨水的硼同位素组成指代中更新世以来东亚夏季风的变化。与黄土高原的黄土相比, 东北地区的酸溶相黄土的硼含量 (0.26 - 0.89 $\mu\text{g/g}$) 较低, 而具有较高的 B 值 (-12.1‰ 至+9.4‰)。利用反演计算三个源区量化各源区供给的硼比例。结果显示, 黄土-古土壤中的硼元素主要来自大气降水和硅酸盐风化。中国东北和黄土高原地区, 在大的空间范围和时间尺度上都可以观察到重建的 Bpr 与其他指标的同步变化。Bpr 与 EASM 的强相关性归因于在含水水汽团输送路径上与气-沉淀相分离相关的硼同位素动力学分馏。提出一种与温度无关的瑞雷分馏模型, 用于解释多步分馏过程中水蒸气损失的 Bpr。基于 Bpr 的季风记录显示 430 ka 左右发生明显变化, 指示 MBE 之后东亚夏季风突然减弱, 这为响应 MBE 的季风演化区域差异提供了依据。北半球的冰量是控制 800 kyr 以来中国东北地区 EASM 变化的因素之一。

ABSTRACT: Based on a study of the boron (B) isotope geochemistry of the loess-paleosol sequence of the Niuyangzigou section (NYZG) in Northeast (NE) China, the boron isotopic composition of paleo-rainwater (Bpr) is used for the first time as a potential proxy for tracing changes in the East Asian summer monsoon (EASM) since the mid-Pleistocene. The acid-soluble phase of loess in NE China, which is characteristically a sandy loess, has lower boron concentrations (0.26 to 0.89 $\mu\text{g/g}$) and more positive B values, from -12.1‰ to +9.4‰, compared to the loess of the Chinese Loess Plateau (CLP). According to the mass balance of boron accumulation from three distinct sources, a mathematical inversion calculation is used to quantify the proportion of boron from each source and to capture the original Bpr signature. The resulting Bpr values range from $+6.8 \pm 0.95\%$ in loess layers to $+17.3 \pm 3.32\%$ in paleosol layers, and the boron accumulated in loess-paleosol layers is shown to be mainly from atmospheric precipitation and silicate weathering. Synchronous variations of reconstructed Bpr and other loess-based proxies, both in NE China and in the CLP, are observed over a large spatial range and on several temporal scales. The linkage of Bpr to the intensity of the EASM is attributed to the kinetic boron isotope fractionation associated with vapor-precipitate phase separation along the transport path of moisture-bearing air masses. A Rayleigh fractionation model is proposed to interpret Bpr in terms of the proportion of water vapor loss after multi-step fractionation processes, which is independent of temperature. The monsoon

record based on Bpr shows a significant shift at ~430 ka, implying an abrupt weakening of the EASM after the Mid-Brunhes Event (MBE), which provides evidence for regional disparities in monsoon evolution in response to the MBE. The ice volume in Northern Hemisphere is a possible factor controlling changes in the EASM in NE China over the past 800 kyr.

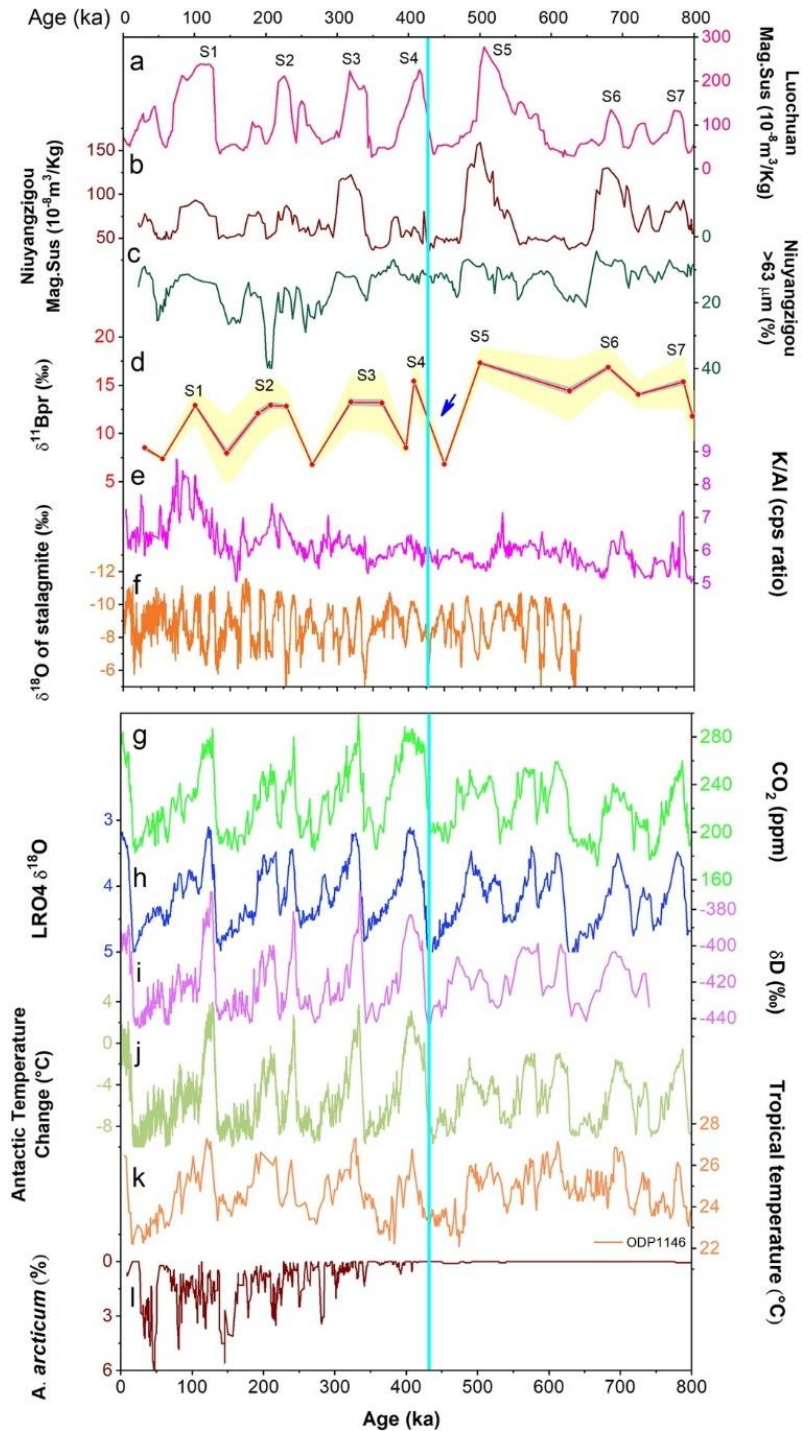


Figure 1. Comparison of the $\delta^{11}\text{Bpr}$ record of loess in NE China with other records over the past 800 kyr. (a) and (b) MS records of the LC (Lu et al., 2004) and NYZG sections (Zeng et al., 2011). (c) Content of coarse particles ($> 63 \mu\text{m}$) in the NYZG section (Zeng et al., 2011). (d) Reconstructed $\delta^{11}\text{Bpr}$ for the

NYZG section (this study). The light yellow shading represents the 2σ analytical error and the light gray shading represents the average values at the 95% confidence level. (e) K/Al ratio of marine sediments in the South China Sea (Tian et al., 2011). (f) $\delta^{18}\text{O}$ of cave sediments in central China (Cheng et al., 2016). (g) Atmospheric CO_2 concentration (Lüthi et al., 2008). (h) LR04 stacked benthic $\delta^{18}\text{O}$ record (Lisiecki and Raymo, 2005). (i) δD record from the EPICA Dome C Antarctic ice core (3,000-yr averages) (EPICA Community Members, 2004). (j) Antarctic temperature changes (Jouzel et al., 2007). (k) SST record from ODP Site 1146 based on alkenone paleotemperature determinations (Herbert et al., 2010). (l) Relative abundance of sea-ice related ostracode species *Acetabulastoma arcticum*, a parasitic species living on the sympagic epipelagic amphipod *Gammarus* in cores from the Western Arctic Ocean (Cronin et al., 2017).

13. 重新定义全球变暖的威胁：气候变化、粮食危机和社会崩溃的经验因果循环图



翻译人：郑威 11930589@mail.sustech.edu.cn

Richards C E, Lupton R C, Allwood J M. *Re-framing the threat of global warming: an empirical causal loop diagram of climate change, food insecurity and societal collapse*[J]. *Climatic Change*, 2021, 164(3): 1-19.

<https://doi.org/10.1007/s10584-021-02957-w>

摘要：人们越来越担心气候变化给人类带来生存风险。了解这些最坏的情况对良好的风险管理至关重要。然而，我们对气候变化可能导致社会崩溃的机制认识还不够成熟。本文旨在确定和构建气候变化、粮食危机和社会崩溃路径的实验性证据。我们首先回顾了社会崩溃和生存危机的文献并且定义了一系列社会崩溃的决定因素。我们开发了一种独创的方法，将这些因素作为社会崩溃的代用指标来确定当代社会的气候变化、粮食危机和社会崩溃的实验性证据，然后在全球和国家尺度上使用一个新形式的因果循环图来构建它。由此产生的证据基于研究的时空分布和数据驱动方法类型而变化。因果循环图记录了证据基础的传播，分别使用线条厚度和颜色来描述数据驱动方法的密度和类型。它有助于探索气候变化的影响如何破坏农业系统和粮食供应，这可能导致经济冲击、社会政治不稳定以及饥饿、人口迁徙和冲突。本文对未来的工作提出了意见以进一步发展我们对气候变化和社会崩溃之间因果路径的定性理解和定量复杂系统建模的能力。

ABSTRACT: There is increasing concern that climate change poses an existential risk to humanity. Understanding these worst-case scenarios is essential for good risk management. However, our knowledge of the causal pathways through which climate change could cause societal collapse is underdeveloped. This paper aims to identify and structure an empirical evidence base of the climate change, food insecurity and societal collapse pathway. We first review the societal collapse and existential risk literature and define a set of determinants of societal collapse. We develop an original

methodology, using these determinants as societal collapse proxies, to identify an empirical evidence base of climate change, food insecurity and societal collapse in contemporary society and then structure it using a novel-format causal loop diagram (CLD) defined at global scale and national granularity. The resulting evidence base varies in temporal and spatial distribution of study and in the type of data-driven methods used. The resulting CLD documents the spread of the evidence base, using line thickness and colour to depict density and type of data-driven method respectively. It enables exploration of how the effects of climate change may undermine agricultural systems and disrupt food supply, which can lead to economic shocks, socio-political instability as well as starvation, migration and conflict. Suggestions are made for future work that could build on this paper to further develop our qualitative understanding of, and quantitative complex systems modelling capabilities for analysing, the causal pathways between climate change and societal collapse.

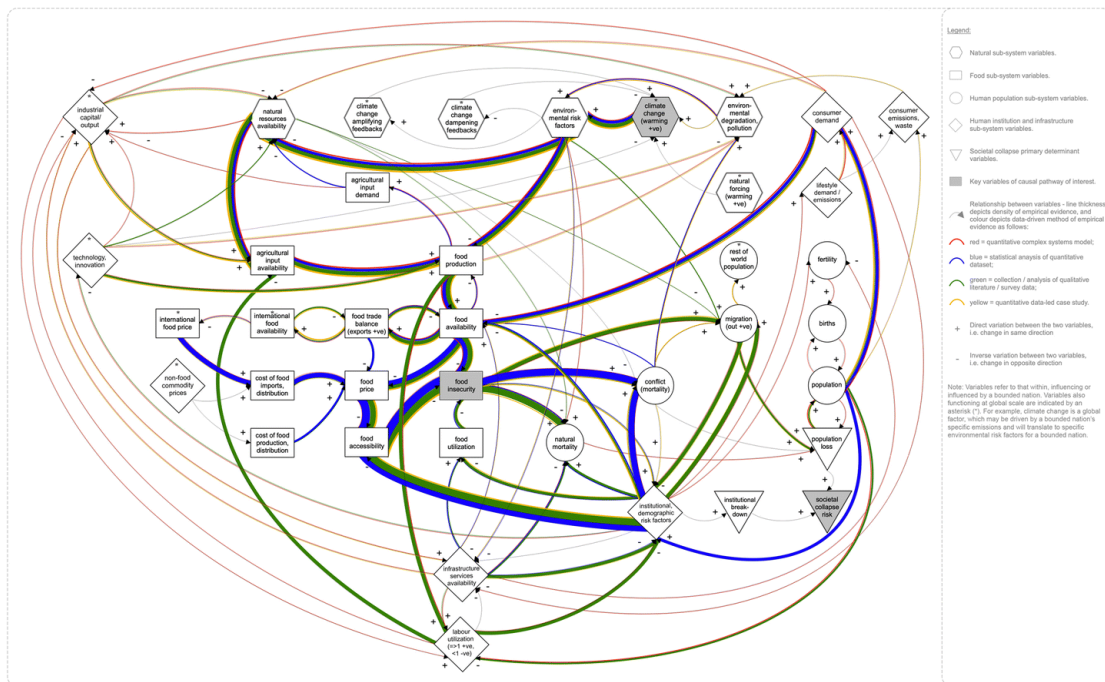


Figure 1. Causal loop diagram of climate change, food insecurity and societal collapse in contemporary society at global scale and national granularity. Variables are depicted as nodes in five different shapes, indicating different sub-systems. Links between variables are depicted as arrowed lines, indicating the direction of the relationship. Each link has a positive (+) or

negative (–) notation, indicating that the two variables change in the same direction or opposite direction, respectively. The density and type of data-driven method of the empirical evidence base, from which the causal loop diagram was constructed, are depicted by line thickness and colour, respectively.